the FEBS Journal

Morphological restriction of human coronary artery endothelial cells substantially impacts global gene expression patterns

Jessica M. Stiles[1,*], Robert Pham[2,*], Rebecca K. Rowntree[1], Clarissa Amaya[1], James Battiste[3], Laura E. Boucheron[2], Dianne C. Mitchell[1] and Brad A. Bryan[1]

1 Department of Biomedical Sciences, Paul L. Foster School of Medicine, Texas Tech University Health Sciences Center, El Paso, TX, USA
2 Klipsch School of Electrical and Computer Engineering, New Mexico State University, Las Cruces, NM, USA
3 Department of Neurology, University of Texas Southwestern Medical Center, Dallas, TX, USA

Keywords
actin; cell morphology; coronary artery; cytoskeleton; endothelial cell; genomics; image recognition; microarray; micropatterning

Correspondence
B. A. Bryan, Center of Excellence in Cancer Research, Paul L. Foster School of Medicine, Texas Tech University Health Sciences Center, 5001 El Paso Drive, MSB1 Room 2111, El Paso, TX 79905, USA
Fax: +1 915 783 5222
Tel: +1 915 783 5235
E-mail: brad.bryan@ttuhsc.edu

*These authors contributed equally to this work.

(Received 7 March 2013, revised 6 May 2013, accepted 24 June 2013)

doi:10.1111/febs.12410

Alterations in cell shape have been shown to modulate chromatin condensation and cell lineage specification; however, the mechanisms controlling these processes are largely unknown. Because endothelial cells experience cyclic mechanical changes from blood flow during normal physiological processes and disrupted mechanical changes as a result of abnormal blood flow, cell shape deformation and loss of polarization during coronary artery disease, we aimed to determine how morphological restriction affects global gene expression patterns. Human coronary artery endothelial cells (HCAECs) were cultured on spatially defined adhesive micropatterns, forcing them to conform to unique cellular morphologies differing in cellular polarization and angularity. We utilized pattern recognition algorithms and statistical analysis to validate the cytoskeletal pattern reproducibility and uniqueness of each micropattern, and performed microarray analysis on normal-shaped and micropatterned HCAECs to determine how constrained cellular morphology affects gene expression patterns. Analysis of the data revealed that forcing HCAECs to conform to geometrically-defined shapes significantly affects their global transcription patterns compared to nonrestricted shapes. Interestingly, gene expression patterns were altered in response to morphological restriction in general, although they were consistent regardless of the particular shape the cells conformed to. These data suggest that the ability of HCAECs to spread, although not necessarily their particular morphology, dictates their genomics patterns.

Introduction

Regulation of the vascular system is essential for tissue growth and homeostasis, and aberrant vascular signalling has been implicated in a vast number of diseases, such as cancer, diabetes, arthritis, macular degeneration and cardiovascular disorders [1]. The majority of research examining endothelial function has focused on the effects of secreted growth factors and cytokines such as vascular endothelial growth factor, fibroblast growth factor, transforming growth factor (TGF)β and a host of other molecules on endothelial cell signalling and physiology. Although these factors undoubtedly play a critical role in regulating cardiovascular development, function and disease, a growing number of studies indicate that

Abbreviations
DAPI, 4′,6-diamidino-2-phenylindole; HCAEC, human coronary artery endothelial cell; KS, Kolmogorov–Smirnov; TGF, transforming growth factor; Wnt, wingless-type.

FEBS Journal **280** (2013) 4474–4494 © 2013 The Authors. FEBS Journal published by John Wiley & Sons Ltd on behalf of FEBS
This is an open access article under the terms of the Creative Commons Attribution-NonCommercial License, which permits use, distribution and reproduction in any medium, provided the original work is properly cited and is not used for commercial purposes.

endothelial physiology, as well as that of many other cell types, is directed by an intimate combination of physical, chemical and biological cues present in the tissue microenvironment [2,3]. Over a century ago, physical cues were hypothesized to play important roles in tissue development and there are no better examples in the human body than the deleterious effects of microgravity on bone structure [4] and hypertension on cardiovascular function [5]. However, almost all organisms have evolved specific structures that are tailored to respond to nano- and macroscale physical forces whereby cells are able to detect and respond to external forces through mechanically induced conformational or organizational changes in cellular molecules, such as stretch-sensitive ion channels, G protein coupled receptors, tyrosine kinase receptors, cadherins and integrins located on the plasma membrane and in cell-to-cell and cell-to-extracellular matrix junctions [6].

Over the past decade, a large number of studies have manipulated endothelial tension, compression and shear stress aiming to determine how mimicking blood flow affects endothelial function [7]. Despite the progress made in this area, many of the mechanisms regulating how extrinsic mechanical stresses affect endothelial physiology remain unknown, and the implications of such studies are primarily limited to extrapolations of how lumenal blood flow from normal, hypertensive and sclerotic conditions affects endothelial cells. A wealth of primarily qualitative evidence suggests that cell morphology-specific regulation of mechanotransduction is essential for cellular fate decisions such as proliferation, apoptosis, differentiation and quiescence [8–12]. For example, restriction of endothelial cell spreading using micropatterned substrates induces cell cycle arrest and apoptosis [8]. Alternatively, cell proliferation increases when cell spreading is allowed, whereas cells preferentially undergo differentiation in a moderately spread state. Endothelial migration is significantly more guided and regulated on narrower adhesive surfaces than on larger ones and geometric cues have been shown to modulate endothelial differentiation [13]. Other cells types may show distinct phenotypes solely on morphological alterations. For example, it has been reported that human stem cells can be directed to osteogenic or adipogenic developmental lineages by simply manipulating cell shape and thereby altering cellular mechanics [14], although more recent follow-up studies conducted in a separate laboratory suggest that adipogenic potential is not dependent on cell geometry [15]. Previously reported data obtained in our laboratory and others indicate that alterations in cell shape and cytoskeletal dynamics are capable of markedly overriding external mitogenic signalling [12,16]. This suggests that, as opposed to a model in which cell proliferation, death and differentiation are largely independent of cell shape, these processes are coordinately regulated and modulated by cellular mechanics. Thus, the local differentials in growth factors, biochemistry and internal and external mechanical stress synergize to modulate the specificity that drives tissue heterogeneity during development, normal function and disease.

Cell shape changes have been associated with nuclear shape remodelling [11,17–19]. It has been hypothesized that the transduction of mechanical information through cytoskeletal/nuclear coupling results in alterations that modulate chromosomal architecture and subsequent accession of transcription factors to their target genes [20–24]. Indeed, recent work has demonstrated that large-scale changes in cell shape induce alterations in chromosome condensation leading to marked effects on cell proliferation [25]. Thus, distinct cellular morphologies may drive the patterning of unique cytoskeletal architectures that govern global gene expression [26]. Despite these findings, it is not known how cell shape and its effects on cytoskeletal structures modulate global transcriptional patterns.

Although the normal surface of arteries is smooth, atherosclerotic arteries are characterized by irregular arrangement of endothelial cells, compromised monolayer integrity, irregular protrusions in the shape of scales or plates, and altered endothelial cell geometry [27,28]. Thus an understanding of how endothelial cell shape changes affect cellular function may shed light on the deregulation of endothelial cells during aberrant states such as hypertension, arteriosclerosis and coronary artery disease. In the present study, we examined the global gene expression changes that occur when human coronary artery endothelial cells (HCAECs) are shape and spread restricted by micropatterning into reproducibly unique cellular morphologies that are distinctive in polarization, morphological angularity and actin cytoskeleton patterning. Given the wealth of data suggesting that cell shape and cytoskeletal patterning can alter cellular physiology across a large number of cell types, we specifically investigated whether unique alterations in these cellular properties are capable of modulating global gene expression changes in endothelial cells. Our data demonstrate that geometric restriction induces dramatic alterations in the HCAEC transcriptome, although these changes are independent of the exact cell shape and/or actin orientation assumed by the cell.

Results

Quantitative analysis of cell shape-induced cytoskeletal and nuclear changes in HCAECs

To determine how cell shape alterations regulate the endothelial transcriptome, we must first utilize a system that manipulates cellular morphology at the same time as consistently maintaining all other growth variables. Accordingly, we seeded HCAECs on collagen I-coated spatially defined micropatterns, allowing cells to adapt to reproducible large (1600 μm^2) geometric patterns, including a disc, crossbow, H, Y and L (Fig. 1A). We specifically utilized this cell type because endothelial cells of the coronary artery are constantly exposed to cyclic mechanical changes from blood flow during normal physiological processes and disrupted mechanical changes as a result of abnormal blood flow, cell shape deformation and loss of polarization during coronary artery disease. The size of the micropattern was specifically chosen because we tested micropatterns restricting the cells to either 700 or 1100 μm^2; however, at these sizes, the cells failed to reproducibly conform to the intended shape (data not shown). Moreover, larger micropatterns would allow multiple cells to attach to one micropattern, thus dramatically affecting reproducibility of cell shape. As a control for nonrestricted morphology, cells were also plated at subconfluent levels on the chip in an area coated in collagen I. These patterns were specifically chosen for their ability to alter cell polarization (because this affects stress fibre architecture and nuclear orientation) [25] and the angularity of the cells' morphologies. Disk-shaped cells adopted a round morphology with obtuse cellular edges and random polarization. Crossbow and H-shaped cells exhibit a combination of obtuse and acute edges and become strongly and moderately polarized, respectively. Y- and L-shaped cells were dominated by acute angles, with strong polarization in the Y-shaped cells and no polarization in the L-shaped cells.

To quantify how endothelial cell shape drives actin cytoskeleton patterning, we performed immunofluorescent confocal imaging of normally-shaped and micropatterned HCAECs labelled with rhodamine-conjugated phalloidin (which stains the actin cytoskeleton), phosphorylated focal adhesion kinase (which stains cellular attachments to the extracellular matrix) and 4′,6-diamidino-2-phenylindole (DAPI) (which highlights the nucleus) (Fig. 1B). For a full understanding of the quantitative differences in the actin cytoskeletal orientation of each immunofluorescent image, we implemented algorithms to separate the structures of interest from the remainder of the image, thus allowing us to describe the image quantitatively rather than using standard qualitative methods. Accordingly, we employed techniques for linear feature extraction to segment and obtain orientation and length of the actin fibres from each image. The techniques included preprocessing the images to enhance foreground elements, actin fibre detection using

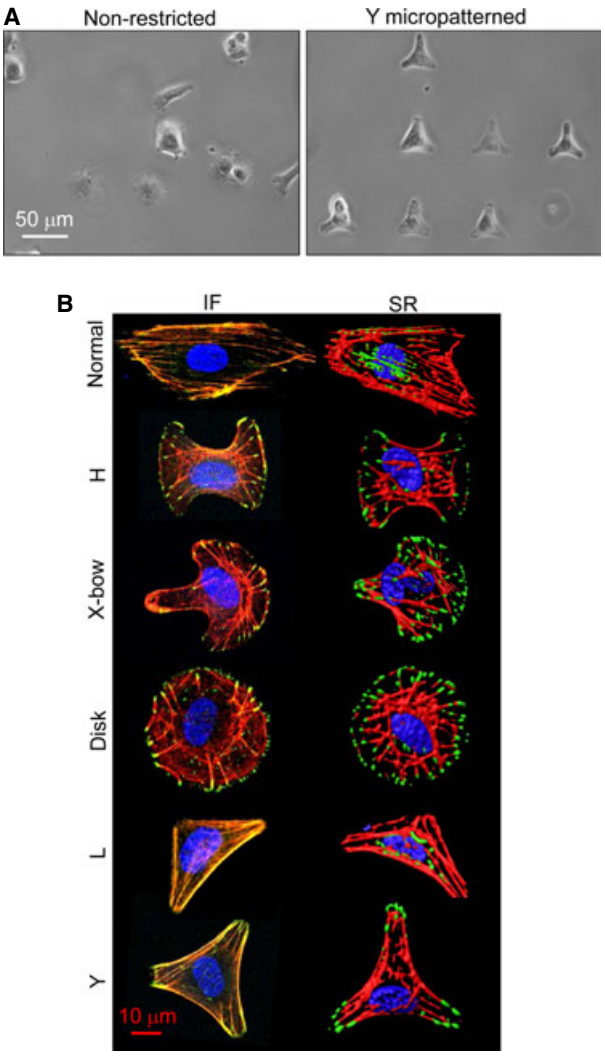

Fig. 1. HCAEC growth on micropatterned substrates. (A) Representative bright field images of HCAECs grown on a nonrestrictive collagen I-coated substrate (normal-shaped) or on collagen I-coated micropatterns (Y shape is represented). Although the micropatterned cells were spatially restricted, HCAECs were seeded at low densities in the nonrestricted controls to ensure minimization of cell-to-cell contacts. (B) Representative immunofluorescence (IF) and surface rendering (RF) images of nonrestricted and micropatterned (H, X-bow, disc, L and Y) HCAECs stained for actin (red), phospho-focal adhesion kinase (green) and nuclei (blue).

FIBERSCORE [29] and filtering including thresholding and mathematical morphology (Fig. 2). Figure 2B provides a more suitable input image to FIBERSCORE for detection because the actin fibres are brighter and display higher contrast. Figure 2C,D shows the correlation and orientation outputs of FIBERSCORE and is used for further analysis of length and orientation, respectively.

We first statistically analyzed the actin fibre orientations using images similar to those shown in Fig. 2D to quantitatively illustrate that HCAECs conforming to one micropatterned shape are indeed unique in cytoskeletal organization compared to those of another micropatterned shape. Immunofluorescent actin images from each shape were tiled into grid regions and the two-sample Kolmogorov–Smirnov (KS) test [30] was utilized to determine whether fibre orientation between cell shapes is truly unique and reproducible in structure (Table 1). High scores (closer to 1.0) occur when actin fibre orientations are largely dissimilar between cells and were observed across shape to shape comparisons. With the exception of normal-shaped cells (which demonstrated high actin orientation variability), we find relatively low rejection scores when comparing all the individual cells with their underlying cumulative tiling, meaning that cells of the same shape have fibre orientations more similar to each other than to other shapes. Note that these comparisons are not symmetric (e.g. comparing X-bow to disk yields slightly different scores than disk to X-bow). This asymmetry is a result of the fact that the orientation of individual images is being compared to the cumulative histogram of a specific shape; we are thus comparing individual disk image fibre orientations with the

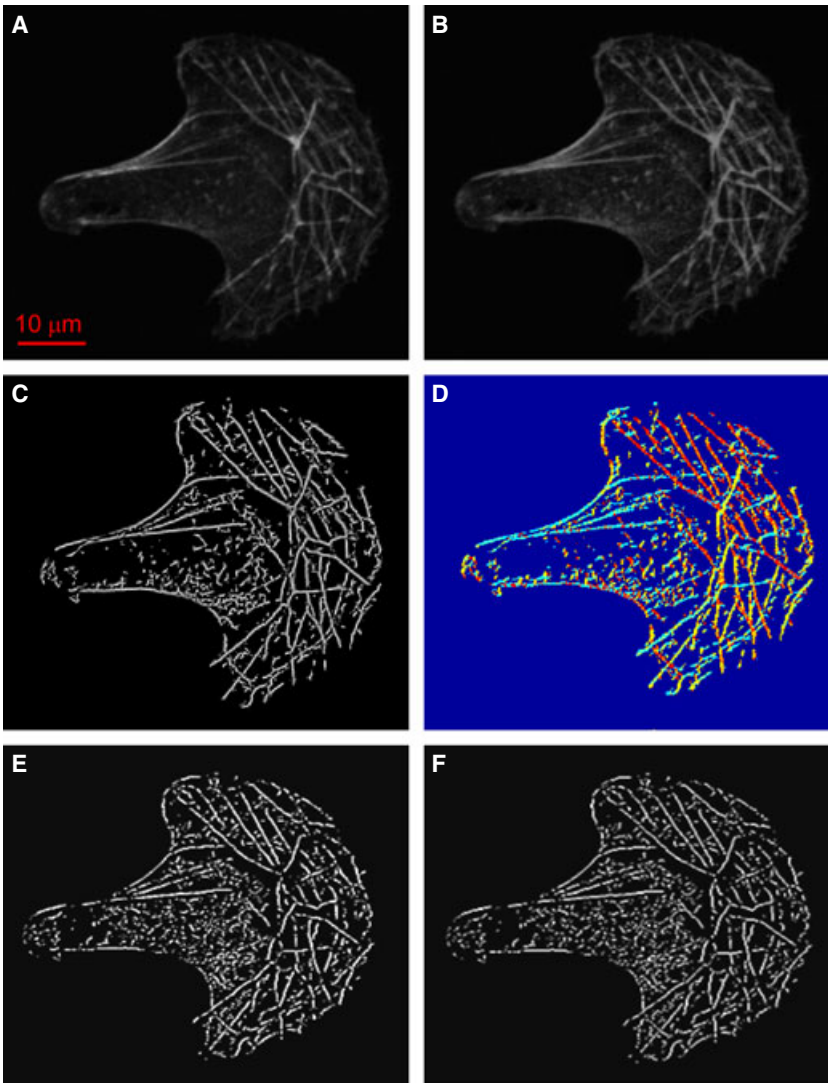

Fig. 2. Cytoskeletal image processing. Actin cytoskeleton images were processed as described in the Materials and methods. The processed images for a X-bow-shaped cell are shown. (A) Original immunofluorescence image in greyscale. (B) Preprocessing: contrast-limited adaptive histogram equalization. (C) Correlation image result from detection with FIBERSCORE. (D) Orientation image result from detection with FIBERSCORE. (E) Postprocessing: threshold. (F) Postprocessing: skeleton.

Table 1. Correlation of actin fibre orientation between each shape. The data presented are the mean scores of the output via a two-sample KS test (scale of 0 to 1 where 1 completely rejects the null hypothesis of the test).

	Crossbow	Disk	H-cell	Y-cell	L-cell	Normal cell
Crossbow	0.54	0.93	0.94	0.68	0.96	0.95
Disk	0.96	0.78	0.95	0.99	0.91	0.99
H-cell	0.93	0.91	0.6	0.93	0.75	0.95
Y-cell	0.71	0.99	0.94	0.5	0.95	0.96
L-cell	0.99	0.95	0.88	0.97	0.39	0.93
Normal cell	0.95	1	0.89	0.95	0.88	0.86

cumulative X-bow orientations and *vice versa*. These comparisons will yield similar but not identical results. These findings strongly validate the idea that the cellular morphologies induced by the micropatterned substrates result in reproducibly unique actin orientations between cell shapes. The analysis of shapes using the tiled grid regions, however, shows similarities in certain regions of a cell between shapes. Detailed analysis of the dominant and second dominant angles in actin orientation between cell shapes revealed that (a) crossbow-shaped cells have more contribution from actin angles close to 0° along the horizontal projection and angles oriented in opposite directions when comparing the widest regions of the crossbow with the narrowest regions; (b) disk-shaped cells have a more uniform distribution of actin angle orientations; (c) H-shaped cells have more contributions from angles close to 0° along the vertical centre; and (d) Y- and L-shaped cells display non-uniform orientation distributions each with a different dominant angle (Fig. 3A–C). This 3×3 tiling is applied in the same manner to all images; the consistency in the KS test results indicate the robustness of the results with respect to this choice of tiling. Note that in regions where it appears that there are no fibres and thus no orientation information (e.g. Y-shape left upper and lower corners) as a result of image variation, we do obtain a small amount of orientation information, as shown in Fig. 3C. We then analyzed the median fibre length using images similar to Fig. 3C between normal and micropatterned HCAECs using the previously described modified FIBERSCORE analysis. As indicated in Fig. 3D, the median fibre length ($\pm$ SEM) for normal-shaped HCAECs was significantly greater (6.84 ± 0.9 μm) than for crossbow- (2.9 ± 0.1 μm), disk- (3.3 ± 0.2 μm), H- (2.6 ± 0.2 μm), Y- (2.9 ± 0.3 μm) and L- (4.3 ± 0.4 μm) shaped cells. Thus, these data strongly indicate that actin orientation and length are truly unique between each cell shape and, if genomic alterations are truly shape and actin confirmation dependent, this model system is sufficient in both design and reproducibility to identify those changes.

Using shape-engineered endothelial cells on circular, square and various rectangular adhesive micropatterns mimicking elongated bipolar shapes, Versaevel *et al.* [25] indicated that cell elongation and spreading is a key parameter of nuclear deformation and this process is absolutely dependent on lateral compressive forces generated by an actomyosin-mediated mechanism. It was further demonstrated that cell elongation leads to successive changes in the level of chromatin condensation as the nuclear shape index is decreased. To test whether changes in cell shape in general (as opposed to solely cell elongation, as shown previously) [25] induce nuclear deformation, we analyzed top and side images of the nuclei from normal and micropatterned HCAECs using confocal microscopy (at least 40 nuclei per condition). The prototypical HCAEC nucleus is ~ 15–18 μm long by 5–8 μm high and maintains a distinctive oval appearance (Fig. 4A, left), whereas deformed nuclei show variability from this norm, as shown in Fig. 4A (middle and right). Although irregularity in nuclear shape occurred relatively infrequently in normal-shaped cells (~ 6% of the cells exhibited nonprototypical nuclei), the percentages were significantly higher in the micropatterned HCAECs, ranging from just over 20% of the L- and Y shaped cells to approximately three-quarters of the population in disc shaped cells (Fig. 4B).

Morphological restriction in HCAECs results in large-scale changes in endothelial global gene transcription independent of the unique shape adopted

Distinct micropattern-mediated alterations in cell shape have been shown to affect lineage specification in mesenchymal progenitor cells [14], although less is known regarding how changes in cell morphology affect terminally differentiated cell types (such as an endothelial cells). Thus, we sought to address two questions: (a) does morphological restriction affect endothelial global transcription and (b) does a distinct cellular morphology uniquely affect endothelial global transcription. Using the reproducible micropatterning system described above, we can effectively address both questions.

We performed whole genome microarray analysis on total RNA collected from nonrestricted and micropatterned HCAECs cultured on 96-well collagen I-coated micropatterned plates and grown in standard growth media. The nonrestricted cells were grown at low

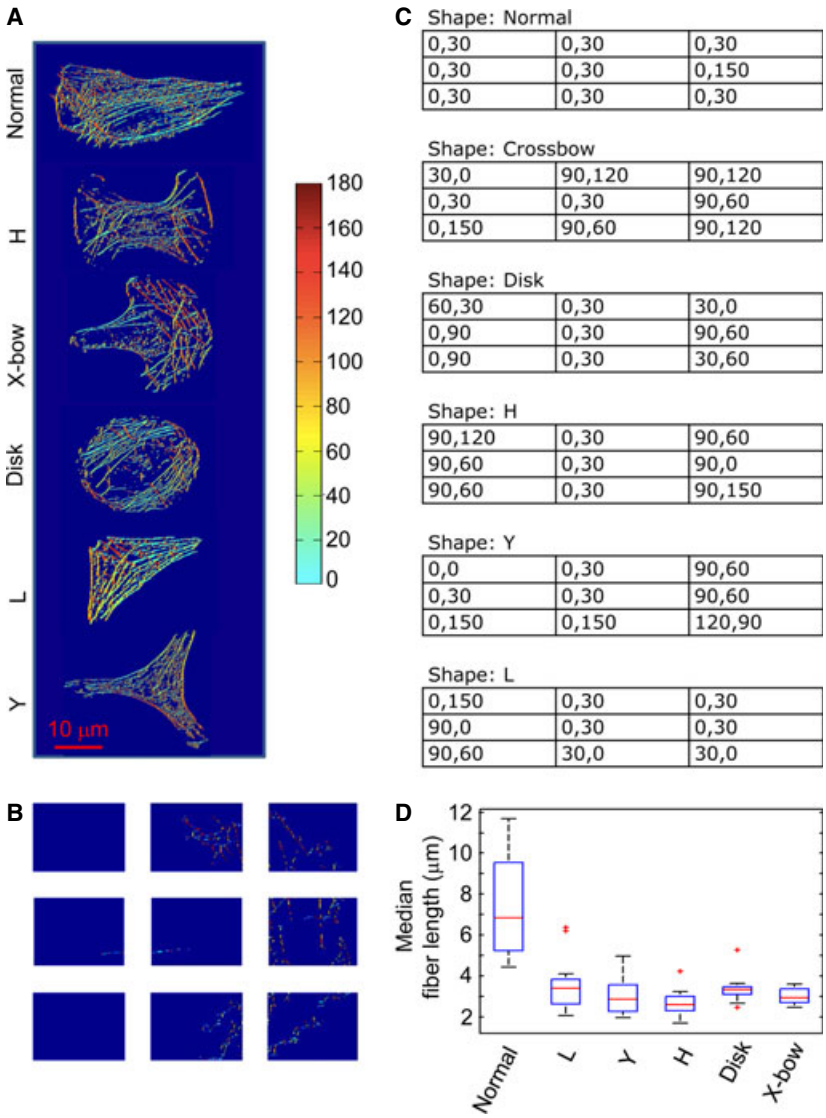

Fig. 3. Quantification of actin fibre orientation and length in normal and micropatterned HCAECs. (A) FIBERSCORE: orientation heatmaps depicting actin orientation for normal and micropatterned HCAECs in relation to their cellular axis. An angle starting at 0° is coincident with the *x*-axis and increases in a counter clockwise direction to 180°. (B) Representative 3 × 3 tiling of a crossbow-shaped HCAEC orientation heatmap. (C) Dominant and second dominant fibre angles in each grid block for each shape. The dominant and second dominant angles are calculated by combining angle information in all images of the particular shape tile. Angles are detected using the restricted angle resolution of FIBERSCORE. (D) FIBERSCORE: correlation quantification of the median fibre length of the actin fibres from normal and micropatterned HCAECs. At least 11–14 images were analyzed from each condition.

confluence to minimize cell-to-cell contacts. Our data revealed large-scale alterations in gene expression as a result of HCAEC morphological restriction. As shown in Fig. 5A,B and Table 2, 361 statistically relevant gene expression changes were equal or greater than two-fold in magnitude ($P < 0.05$) in at least one of the cell shapes compared to normally-shaped HCAECs cells cultured on the same micropatterned plate. The complete data set is publically available via the Gene Expression Omnibus (http://www.ncbi.nlm.nih.gov/geo) (accession number GSE43349). These results provide strong evidence that restricting cell shape induces changes in the global transcriptional patterns of endothelial cells.

Although seeding density was controlled in these experiments to minimize cell-to-cell contact (particularly in the control samples where cellular interactions are possible), it is probable that the use of rich growth media encourages the proliferation of the nonrestricted cells but, because shape restriction has been shown to inhibit proliferation [8], is unable to do so in the shape-restricted cells. This could potentially induce bias in the interpretation of the data from the unrestricted HCAECs as a result of differences in cell cycle progression or cell-to-cell contacts that arise between the mother and daughter cells following mitosis. To address this potential concern, we performed the same micropatterning experiment as described above, except the cells in both the nonrestricted and shape-restricted conditions were serum starved for 48 h before RNA collection to block cell proliferation, thus eliminating variables such as cell-to-cell contact, cell cycle

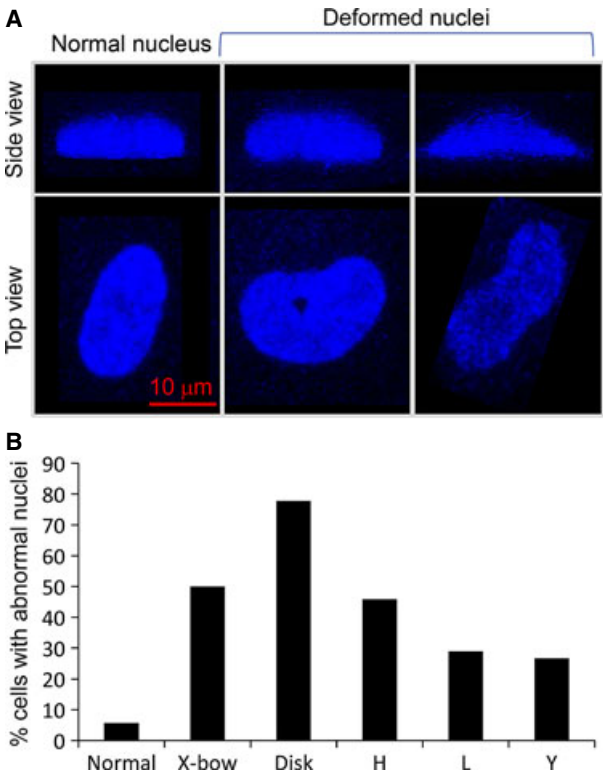

Fig. 4. Micropatterning of HCAECs increases the incidence of nuclear deformation. (A) Confocal top and side images of DAPI-stained HCAEC nuclei. The prototypical normal nucleus is shown in the left panel, whereas examples of deformed nuclei are shown in the middle and right panels. (B) Percentage of the cell population exhibiting a deformed nucleus. At least 40 nuclei were counted for each condition.

differences, etc. A comparison of the profile plots of nonrestricted versus shape-restricted HCAECs grown in standard growth conditions or subsequent to serum starvation yielded similar results, indicating that, regardless of growth conditions, proliferation or cell-to-cell contact, morphological restriction induced significant changes in the global gene expression profiles (Fig. 5C). The complete microarray data set for the serum starvation experiment is publically available via the Gene Expression Omnibus (accession number GSE44168).

Previous data collected from mesenchymal progenitor cells conforming to micropatterns that induced the cells to form obtuse versus acute morphological angles suggested that cell morphology controls lineage specification. Although endothelial cells are terminally differentiated, we aimed to determine whether such distinct morphological as well as polarity changes might influence the endothelial transcriptome. By excluding the nonrestricted conditions from the analysis, we compared the gene expression changes between only the micropatterned endothelial cells adhering to cross-bow, disc, H, L and Y shapes to examine whether distinct cellular morphology can affect endothelial gene expression patterns. As shown in Fig. 5B,C and Table 2, gene expression changes did not significantly vary based on the particular shape, actin patterning or polarity to which the cells conformed. Indeed, statistical analysis of the genomic data set failed to reveal a single two-fold or greater ($P < 0.05$) alteration in gene expression between any of the cell shapes. These data suggest that, unlike mesenchymal stem cells whose phenotype can be modulated by cellular angularity, endothelial cells grown under these unique geometric constraints do not differ in their global gene expression patterns. Cumulatively, our data indicates that morphological constraint, rather than cellular angularity and polarity, alter the global transcriptome under these conditions.

Pathway analysis of the morphology induced transcriptome changes

We next implemented a systems level approach to understand how geometric constraint may affect the overall cellular phenotype. Our initial analysis reported above included two-fold or greater changes in gene expression, yet, for this network analysis, we broadened our microarray data set (from the standard growth condition experiment) to include the 1.4-fold or greater statistically relevant ($P < 0.05$) changes in gene expression. This cut-off was selected not only to refrain from limiting our network analysis to solely the highest expression changes, but also to take into account transcriptional changes that were less pronounced but still relevant with regard to modulating cellular physiology. This resulted in ~8% of the human genome experiencing changes in gene expression (642 up-regulated genes and 1218 down-regulated genes). We then performed METACORE pathway analysis of these gene expression changes to predict significant alterations in major cellular processes, including cell cycle regulation ($P < 3.3 \times 10^{-8}$) (Table 3), cytoskeletal dynamics and cell adhesion ($P < 4.2 \times 10^{-5}$) (Table 4), glycolysis/gluconeogenesis ($P < 2.7 \times 10^{-4}$) (Table 5), TGFβ signalling ($P < 1.6 \times 10^{-3}$) (Table 6) and wingless-type (Wnt) signalling ($P < 1.6 \times 10^{-3}$) (Table 7). Because TGFβ signalling has been shown to play a major role in arteriosclerotic disease progression, we confirmed our microarray data utilizing quantitative PCR to detect the shape-induced alterations in mRNA expression levels of the TGFβ signalling genes *SMAD6*, *SMAD7* and *TGFB2*, as well as several genes

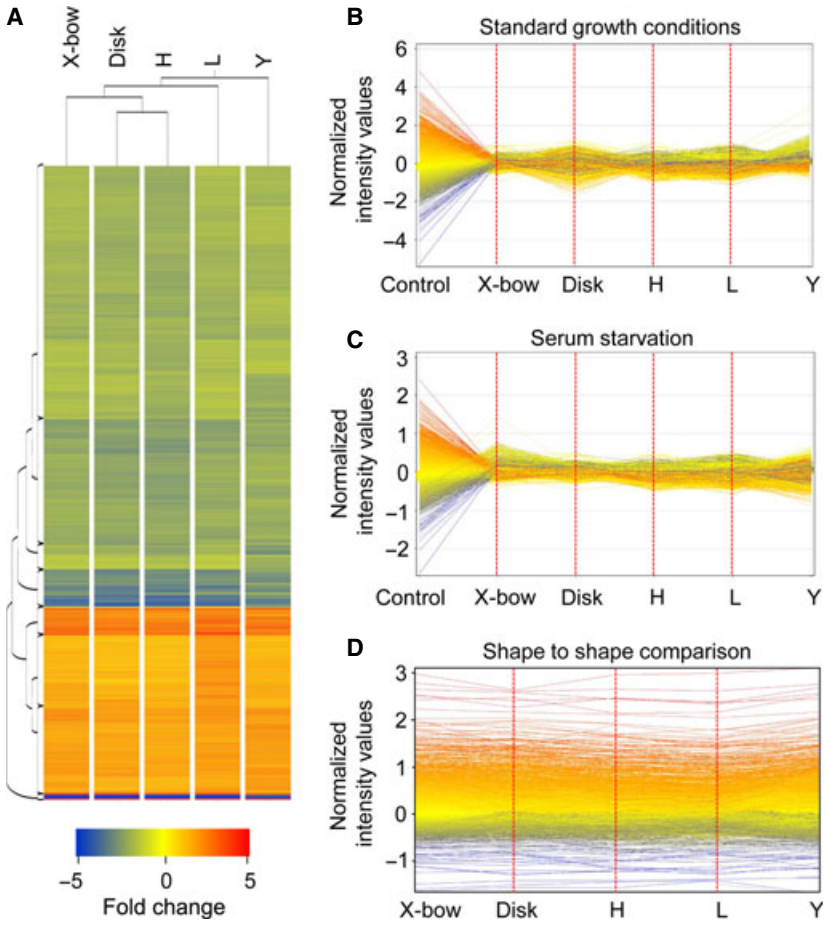

Fig. 5. Global changes in gene expression between normal and micropatterned HCAECs. (A) Hierarchical clustering and heatmap representation of the 361 genes differentially expressed in the shape-restricted cells compared to the nonrestricted controls. The colour-coded scale (blue–green = down-regulation; orange–red = up-regulation) for the normalized fold changes is indicated at the bottom. Details for the regulated genes are provided in Fig. 2 and are publically available via the Gene Expression Omnibus (accession number GSE43349). Only genes with expression levels regulated above a two-fold change ($P < 0.05$) compared to the nonrestricted cells are shown. (B, C) Profile plots correlating the gene expression levels based on normalized signal intensities of probe sets between nonrestricted and micropatterned HCAECs under (B) standard growth conditions or (C) after 48 h of serum starvation. (D) Profile plot comparison of the gene expression intensity changes only between each micropattern condition.

reportedly involved in the atherosclerotic process, including *LPL*, *MMP1*, *KDR*, *ITGA2*, *ACE*, *BIRC3*, *IL1R1*, *ICAM1*, *HEY1*, *BCL2*, *CSF2*, *APOE*, *PDGFB*, *BCL2A1*, *CCL2* and *LDLR* (Fig. 6).

Discussion

The interplay between the physical, chemical and biological cues to which cells are constantly exposed modulates processes ranging from those as broad as cellular lineage determination to those as subtle as the functional nuances between two adjacent cells. Despite the number of studies addressing this area of research, the molecular mechanisms by which these cues synergize is largely unknown. It has been reported that cellular morphology and cytoskeletal angularity greatly influence progenitor lineage specification [14] and that changes in cell shape influence chromatin condensation via nuclear deformation [25]. In the present study, we aimed to determine whether morphological changes in coronary artery endothelial cells could affect the global patterns of gene expression. Understanding how cell shape change affects the coronary artery endothelial cell transcriptome may allow us to better understand the molecular aberrations that underlie coronary artery disease. The present study made use of micropatterned growth substrates that force cells to conform to precise geometric shapes. Although micropatterned cell growth has been utilized in a limited number of studies, there is little evidence that such techniques consistently lead to morphological and cytoskeletal patterns that are highly reproducible and truly unique between different micropatterns. We utilized pattern recognition algorithms and statistical analysis to confirm that cells conforming to the crossbow, disk, H, L or Y shapes had truly reproducible cellular morphology and cytoskeletal architecture unique for each cell shape adopted. Given that most analysis of cytoskeletal organization in the available literature is qualitative in nature, this algorithm can be extensively used in the future to provide quantitative interpretations of the differences in both static (as we have analyzed) and dynamic cytoskeletal structures between two or more treatment groups.

Table 2. Two-fold or greater alterations in gene expression compared to normal-shaped coronary artery endothelial cells (standard growth media).

Gene symbol	Gene name	Accession number	X-bow	Disc	H	L	Y
TMEM100	Transmembrane protein 100, TV2	NM_018286.2	6.4	5	6.3	6.4	7
PTGS2	Prostaglandin-endoperoxide synthase 2	NM_000963.1	4.3	3.7	4	3.9	4.1
IRF6	Interferon regulatory factor 6	NM_006147.2	3.4	2.9	2.8	3	3.5
ALPL	Alkaline phosphatase, liver/bone/kidney, TV1	NM_000478.3	3.3	3.5	3.3	3.4	3.1
C8orf4	Chromosome 8 ORF 4	NM_020130.3	3.2	2.6	3.1	2.7	3
HEY1	Hairy/enhancer-of-split related with YRPW motif 1, TV2	NM_001040708.1	3.1	2.7	2.7	2.7	3.1
BMF	Bcl2 modifying factor, TV2	NM_033503.3	3	3.3	3	2.9	3
BMF	Bcl2 modifying factor, TV4	NM_001003943.1	3	3.1	2.9	2.7	2.9
LOC730525	Hypothetical protein	XM_001126202.1	3	2.8	2.7	3	4
SEMA3G	Semaphorin 3G	NM_020163.1	2.9	3.2	2.6	2.9	2.6
HSD17B11	Hydroxysteroid (17β) dehydrogenase 11	NM_016245.2	2.9	2.2	2.6	2.5	3.3
F2RL3	Coagulation factor II (thrombin) receptor-like 3	NM_003950.2	2.8	2.8	2.7	2.9	2.6
TOX2	TOX high mobility group box family member 2, TV4	NM_001098796.1	2.8	3.1	2.7	2.4	2.6
C20orf100	TOX high mobility group box family member 2	NM_032883.1	2.8	2.6	2.4	2.3	3.1
TOX2	TOX high mobility group box family member 2, TV1	NM_001098797.1	2.8	2.8	2.6	2.3	2.9
SPRY1	Sprouty homologue 1, antagonist of FGF signalling (*Drosophila*), TV1	NM_005841.1	2.7	2.5	2.7	2.6	3.3
SPRY1	Sprouty homologue 1, antagonist of FGF signalling (*Drosophila*), TV2	NM_199327.1	2.7	2.4	2.7	2.7	3.1
ZBTB16	Zinc finger and BTB domain containing 16, TV2	NM_001018011.1	2.6	2.6	2.6	2.7	2.7
TMEM140	Transmembrane protein 140	NM_018295.2	2.6	2.2	2.3	2	2.5
NPTX1	Neuronal pentraxin I	NM_002522.2	2.6	2.7	2.2	2.1	2.6
SMAD7	SMAD family member 7	NM_005904.2	2.6	2.4	2.5	2.7	2.6
ANKRD1	Ankyrin repeat domain 1 (cardiac muscle)	NM_014391.2	2.5	2.8	2.7	2.7	3.1
CXCR4	Chemokine (C-X-C motif) receptor 4, TV1	NM_001008540.1	2.4	2.5	2.3	2.1	2.5
SYNM	Synemin, intermediate filament protein, TVB	NM_015286.5	2.4	2.1	2	2.2	2.4
HLX	H2.0-like homeobox	NM_021958.2	2.4	2.7	2.2	2	2
EFNB2	Ephrin-B2	NM_004093.2	2.3	2.2	2.1	2	2.2
TNFAIP8L3	Tumour necrosis factor, α-induced protein 8-like 3	NM_207381.2	2.2	2.3	1.9	2	2.2
NEDD9	Neural precursor cell expressed, develop. down-regulated 9 , TV2	NM_182966.2	2.2	1.7	1.9	1.9	2.6
GDF15	Growth differentiation factor 15	NM_004864.1	2.1	2.2	2	1.9	2.1
CALCRL	Calcitonin receptor-like	NM_005795.4	2.1	1.8	2	1.7	2
RDX	Radixin, TV3	NM_002906.3	2.1	1.9	1.9	1.6	2.1
MMP10	Matrix metallopeptidase 10 (stromelysin 2)	NM_002425.1	2	2	1.6	1.4	1.7
CMTM8	CKLF-like MARVEL transmembrane domain containing 8	NM_178868.3	2	2	1.8	1.8	2
C13orf15	Regulator of cell cycle	NM_014059.2	2	2	1.8	1.7	2.1
NDRG4	NDRG family member 4	NM_022910.1	2	2.1	1.9	1.7	1.9
LOC100132564	Hypothetical protein	XM_001713808.1	2	2.3	1.4	1.4	2.1
CRYAB	Crystallin, alpha B	NM_001885.1	1.9	1.9	1.7	1.9	2.5
RRAGD	Ras-related GTP binding D	NM_021244.3	1.9	1.6	1.8	1.7	2
IL10	Interleukin 10	NM_000572.2	1.9	1.6	1.4	1.5	2.6
LOC100129211	Hypothetical protein	XM_001718981.1	1.8	1.8	1.5	1.6	2
GRAP	GRB2-related adaptor protein	NM_006613.3	1.8	1.8	1.6	1.6	2
C8orf45	Chromosome 8 open reading frame 45	NM_173518.2	1.8	1.7	1.5	1.6	2.1
PDGFB	Platelet-derived growth factor beta (oncogene homolog), TV1	NM_002608.1	1.8	2.2	2	1.8	2
LOC100190986	Nuclear pore complex interacting protein pseudogene	NR_024456.1	1.8	1.7	1.8	1.6	2.5
PGF	Placental growth factor	NM_002632.4	1.8	2	1.6	1.5	1.6
LOC100132247	Nuclear pore complex interacting protein related gene	NM_001135865.1	1.7	1.4	2.2	1.7	1.9

Table 2. (Continued).

Gene symbol	Gene name	Accession number	X-bow	Disc	H	L	Y
FAM175A	Family with sequence similarity 175, member A	NM_139076.2	1.7	1.4	1.4	1.4	2.1
PDGFB	Platelet-derived growth factor beta (oncogene homolog), TV2	NM_033016.1	1.7	2.1	2.1	1.7	1.7
LOC440353	Nuclear pore complex interacting protein pseudogene	NR_002603.1	1.7	1.5	2.1	1.7	2.1
KIAA1751	KIAA1751	NM_001080484.1	1.6	1.7	1.5	1.5	2.5
LOC613037	Nuclear pore complex interacting protein pseudogene	NR_002555.2	1.6	1.4	2	1.5	2.1
MAGT1	Magnesium transporter 1	NM_032121.4	1.6	1.7	1.7	1.5	2
ZNF738	Misc_RNA, partial miscRNA	XR_040185.1	1.6	1.5	1.4	1.4	2
DMC1	DMC1 dosage suppressor of mck1 homolog	NM_007068.2	1.6	1.7	1.4	1.4	2.4
LOC729978	Similar to LOC339047 protein, TV2	XM_001723016.1	1.6	1.5	1.5	1.3	2
LOC23117	KIAA0220-like protein, TV16	XM_933834.2	1.6	1.5	1.6	1.6	2.1
LOC100132585	Hypothetical protein	XM_001722111.1	1.6	1.5	1.5	1.3	2.2
LOC440348	Nuclear pore complex interacting protein-like 2	NM_001018059.2	1.6	1.7	1.9	1.7	2.1
LOC440345	Hypothetical protein, TV6	XM_933717.1	1.6	1.5	2.1	1.7	2.5
LOC728809	Hypothetical LOC728809	XM_001719546.1	1.6	1.4	1.4	1.3	2
TRIM13	Tripartite motif containing 13, TV4	NM_001007278.1	1.6	1.5	1.6	1.5	2.1
IMAGE:2760091 3	NCI_CGAP_Lu28 Homo sapiens cDNA clone IMAGE:2760091 3	AW276479	1.6	1.4	1.6	1.5	2.5
CATSPER2	Cation channel, sperm associated 2, TV4	NM_172097.1	1.5	1.3	1.4	1.4	2.1
MCART1	Mitochondrial carrier triple repeat 1	NM_033412.1	1.5	1.7	1.3	1.2	2.3
NLRP8	NLR family, pyrin domain containing 8	NM_176811.2	1.5	1.5	1.3	1.4	2.1
LOC255167	Uncharacterized LOC255167	NR_024424.1	1.5	1.6	1.3	1.3	2.2
DDX51	DEAD (Asp-Glu-Ala-Asp) box polypeptide 51	NM_175066.2	1.4	1.3	1.3	1.4	2
C21orf55	Chromosome 21 ORF 55	NM_017833.2	1.4	1.4	1.2	1.3	2.1
LOC90586	Amine oxidase, copper containing 3 pseudogene	NR_002773.1	1.4	1.6	1.4	1.5	2.2
LOC100130168	Hypothetical protein	XM_001719127.1	1.4	1.4	1.2	1.2	2
MAPK8IP3	Mitogen-activated protein kinase 8 interacting protein 3, TV2	NM_001040439.1	1.4	2	1.6	1.6	1.7
ZNF682	Zinc finger protein 682, TV1	NM_033196.2	1.4	1.4	1.3	1.3	2.2
ZNF486	Zinc finger protein 486	XM_371152.3	1.3	1.4	1	1.2	2.1
SULT1A1	Sulfotransferase family, cytosolic, 1A, phenol-preferring, member 1, TV3	NM_177530.1	1.3	1.4	1.4	1.3	2
LOC100128510	Hypothetical protein	XM_001715759.1	1.3	1.5	1.4	1.5	2
LOC653994	Similar to eukaryotic translation initiation factor 4H, TV2	XM_944429.1	−1.3	−2.2	−1.3	−1.5	1
LOC648024	Similar to eukaryotic translation initiation factor 4A, TV1	XR_018316.1	−1.3	−1.8	−1.6	−2.1	−1.3
NDUFA8	NADH dehydrogenase (ubiquinone) 1α subcomplex, 8	NM_014222.2	−1.4	−1.3	−1.7	−2.0	−1.4
TNPO1	Transportin 1, TV2	NM_153188.2	−1.4	−2.3	−1.5	−1.7	−1.3
SNAP23	Synaptosomal-associated protein, 23 kDa, TV1	NM_003825.2	−1.4	−2.0	−1.4	−1.6	−1.3
TCEA1	Transcription elongation factor A (SII), TV2	NM_201437.1	−1.4	−2.0	−1.6	−1.8	−1.4
ALCAM	Activated leukocyte cell adhesion molecule	NM_001627.2	−1.4	−1.4	−1.6	−2.0	−1.8
TCEAL8	Transcription elongation factor A (SII)-like 8, TV2	NM_001006684.1	−1.4	−1.5	−1.7	−2.0	−1.4
TMEM189-UBE2V1	TMEM189-UBE2V1 readthrough transcript, TV2	NM_003349.4	−1.4	−2.0	−1.5	−1.7	−1.3
LOC730052	Misc_RNA (LOC730052)	XR_016054.2	−1.4	−2.0	−1.4	−1.7	−1.3
TXNDC5	Thioredoxin domain containing 5 (endoplasmic reticulum), TV1	NM_030810.2	−1.4	−2.0	−1.4	−1.5	−1.6
BCL2L1	BCL2-like 1, nuclear gene encoding mitochondrial protein, TV1	NM_138578.1	−1.5	−2.0	−1.3	−1.6	−1.3
EIF4G2	Eukaryotic translation initiation factor 4γ, 2, TV1	NM_001418.3	−1.5	−2.2	−1.5	−2.0	−1.5
TCP1	T-complex 1, TV1	NM_030752.2	−1.5	−2.1	−1.4	−1.8	−1.4
CCT6A	Chaperonin containing TCP1, subunit 6A (zeta 1), TV1	NM_001762.3	−1.5	−2.1	−1.5	−1.9	−1.4

Table 2. (Continued).

Gene symbol	Gene name	Accession number	X-bow	Disc	H	L	Y
LOC644063	Similar to heterogeneous nuclear ribonucleoprotein K	XR_016547.1	−1.5	−2.2	−1.6	−2.0	−1.3
LSM5	LSM5 homologue, U6 small nuclear RNA associated (*Saccharomyces cerevisiae*)	NM_012322.1	−1.5	−1.6	−2.0	−1.9	−1.8
FEZ2	Fasciculation and elongation protein zeta 2 (zygin II), TV1	NM_005102.2	−1.5	−1.7	−1.8	−2.1	−1.6
C14orf149	Chromosome 14 ORF 149	NM_144581.1	−1.5	−1.6	−1.8	−2.0	−1.9
LOC728059	Misc_RNA	XR_015606.1	−1.5	−2.4	−1.6	−2.3	−1.7
THOC4	THO complex 4	XM_001134346.1	−1.5	−1.8	−1.6	−2.0	−1.5
LYPLA1	Lysophospholipase I	NM_006330.2	−1.5	−1.9	−1.8	−2.1	−1.5
EDG1	Endothelial differentiation, sphingolipid G-protein-coupled receptor, 1	NM_001400.3	−1.5	−1.5	−1.5	−2.2	−1.6
LOC648695	Similar to retinoblastoma binding protein 4, TV5	XM_944246.2	−1.5	−2.2	−1.8	−2.2	−1.7
MALL	Mal, T-cell differentiation protein-like	NM_005434.3	−1.5	−1.3	−1.7	−2.0	−1.7
ZFAND6	Zinc finger, AN1-type domain 6	NM_019006.2	−1.5	−2.2	−1.6	−1.8	−1.6
ADK	Adenosine kinase, transcript variant ADK-short	NM_001123.2	−1.5	−1.6	−1.9	−2.0	−1.5
ZYX	Zyxin, TV1	NM_003461.4	−1.5	−1.4	−2.0	−1.7	−1.7
PAPSS2	3′-phosphoadenosine 5′-phosphosulfate synthase 2, TV1	NM_004670.3	−1.5	−1.5	−1.7	−2.1	−1.5
G3BP2	GTPase activating protein (SH3 domain) binding protein 2, TV3	NM_203504.1	−1.5	−1.6	−1.6	−2.1	−1.6
LOC100130561	Similar to high-mobility group protein 1-like 10, TV2	XM_001723189.1	−1.5	−2.1	−1.6	−1.9	−1.5
HIGD1A	HIG1 hypoxia inducible domain family, member 1A, TV1	NM_001099668.1	−1.6	−2.0	−1.8	−2.1	−1.7
EPB41L3	Erythrocyte membrane protein band 4.1-like 3	NM_012307.2	−1.6	−1.7	−1.6	−2.0	−1.8
IARS	Isoleucyl-tRNA synthetase, TV short	NM_002161.3	−1.6	−1.5	−1.7	−2.0	−1.5
RRAS2	Related RAS viral (r-ras) oncogene homologue 2	NM_012250.3	−1.6	−1.9	−1.8	−2.0	−1.3
RANBP1	RAN binding protein 1	NM_002882.2	−1.6	−1.6	−2.1	−2.0	−1.7
NOL6	Nucleolar protein family 6 (RNA-associated), TV γ	NM_139235.3	−1.6	−1.3	−2.0	−1.7	−1.5
C18orf55	Chromosome 18 ORF 55	NM_014177.1	−1.6	−1.7	−1.7	−2.1	−1.6
CSE1L	CSE1 chromosome segregation 1-like (yeast)	NM_001316.2	−1.6	−1.6	−1.8	−2.0	−1.6
TIMM23	Translocase of inner mitochondrial membrane 23 homologue	NM_006327.2	−1.6	−1.7	−1.8	−2.1	−1.6
FHL2	Four and a half LIM domains 2, TV4	NM_201557.2	−1.6	−1.6	−1.8	−2.0	−1.6
AP1S1	Adaptor-related protein complex 1, sigma 1 subunit, TV4	NM_057089.2	−1.6	−1.5	−1.9	−2.1	−1.4
HNRPA2B1	Heterogeneous nuclear ribonucleoprotein A2/B1, TV B1	NM_031243.1	−1.6	−1.5	−1.8	−2.0	−1.8
CCNC	Cyclin C, TV2	NM_001013399.1	−1.6	−2.0	−1.7	−1.9	−1.5
PTPLAD1	Protein tyrosine phosphatase-like A domain containing 1	NM_016395.2	−1.6	−1.7	−1.8	−2.1	−1.5
HNRNPK	Heterogeneous nuclear ribonucleoprotein K, TV2	NM_031263.2	−1.6	−1.8	−1.5	−2.0	−1.5
HAT1	Histone acetyltransferase 1, TV1	NM_003642.2	−1.6	−1.7	−2.0	−1.9	−1.7
PSME3	Proteasome (prosome, macropain) activator subunit 3, TV1	NM_005789.2	−1.6	−1.3	−2.0	−2.0	−1.6
HIGD1A	HIG1 hypoxia inducible domain family, member 1A, TV1	NM_001099668.1	−1.6	−1.7	−1.8	−2.1	−1.6

Table 2. (Continued).

Gene symbol	Gene name	Accession number	X-bow	Disc	H	L	Y
ARMCX3	Armadillo repeat containing, X-linked 3, TV2	NM_177947.2	−1.6	−2.0	−1.5	−2.0	−1.6
LOC100128266	PREDICTED: Misc_RNA	XR_038984.1	−1.6	−2.1	−1.8	−2.1	−1.7
DCBLD2	Discoidin, CUB and LCCL domain containing 2	NM_080927.3	−1.6	−1.6	−2.1	−1.9	−1.8
SMS	Spermine synthase	NM_004595.2	−1.6	−1.9	−1.8	−2.0	−1.7
TPM3	Tropomyosin 3, TV1	NM_152263.2	−1.6	−1.9	−1.8	−2.1	−1.4
LOC653884	Similar to FUS interacting protein (serine-arginine rich) 1	XM_936240.1	−1.6	−1.9	−1.6	−2.0	−1.5
ATP5G1	ATP synthase, mitochondrial Fo complex, subunit C1, TV2	NM_001002027.1	−1.6	−1.5	−1.9	−2.0	−1.7
SDCBP	Syndecan binding protein (syntenin), TV2	NM_001007067.1	−1.6	−2.0	−1.6	−2.1	−1.7
MCM6	Minichromosome maintenance complex component 6	NM_005915.4	−1.6	−1.7	−2.0	−2.0	−1.7
BRIX1	BRX1, biogenesis of ribosomes, homologue (*S. cerevisiae*)	NM_018321.3	−1.6	−1.7	−1.7	−2.0	−1.7
RPL29	Ribosomal protein L29	NM_000992.2	−1.6	−2.1	−2.0	−2.2	−1.6
LOC644330	Similar to tropomyosin 3 isoform 2	XR_017492.1	−1.6	−2.0	−1.8	−1.9	−1.6
LPXN	Leupaxin	NM_004811.1	−1.6	−1.6	−1.9	−2.0	−1.8
LOC100130506	Hypothetical protein	XM_001724500.1	−1.6	−1.7	−2.0	−2.0	−1.7
DDX21	DEAD (Asp-Glu-Ala-Asp) box polypeptide 21	NM_004728.2	−1.6	−1.6	−1.7	−2.0	−1.5
LDHA	Lactate dehydrogenase A	NM_005566.1	−1.6	−1.6	−1.9	−2.0	−1.8
LOC642590	Misc_RNA	XR_016251.2	−1.6	−1.7	−2.0	−1.9	−1.7
FKBP14	FK506 binding protein 14, 22 kDa	NM_017946.2	−1.6	−1.7	−1.9	−2.1	−1.6
NME1	NME/NM23 nucleoside diphosphate kinase 1, TV2	NM_000269.2	−1.6	−1.8	−2.1	−2.1	−1.7
AHNAK	AHNAK nucleoprotein, TV1	NM_001620.1	−1.6	−1.6	−2.0	−1.8	−1.4
CKS2	CDC28 protein kinase regulatory subunit 2	NM_001827.1	−1.6	−1.5	−2.0	−2.1	−1.7
CYCSL1	Cytochrome c, somatic-like 1 on chromosome 6	NR_001561.1	−1.6	−2.0	−1.9	−2.1	−1.7
LOC646347	Misc_RNA	XR_017680.1	−1.7	−1.9	−1.9	−2.1	−1.8
WDR4	WD repeat domain 4, TV2	NM_033661.3	−1.7	−1.5	−1.9	−2.2	−1.6
ALDH1A3	Aldehyde dehydrogenase 1 family, member A3	NM_000693.1	−1.7	−1.7	−2.0	−2.4	−1.9
CLINT1	Clathrin interactor 1	NM_014666.2	−1.7	−1.6	−1.8	−2.0	−1.6
GNG12	Guanine nucleotide binding protein (G protein), γ 12	NM_018841.4	−1.7	−2.5	−1.6	−2.1	−1.6
TOMM5	Translocase of outer mitochondrial membrane 5 homologue, TV1	NM_001001790.2	−1.7	−1.7	−2.0	−1.9	−1.9
MPZL2	Myelin protein zero-like 2, TV1	NM_005797.2	−1.7	−1.8	−1.9	−2.2	−1.7
DUSP14	Dual specificity phosphatase 14	NM_007026.2	−1.7	−1.6	−1.9	−2.1	−1.9
IDH1	Isocitrate dehydrogenase 1 ($NADP^+$), soluble	NM_005896.2	−1.7	−2.0	−1.7	−1.9	−1.8
CYTL1	Cytokine-like 1	NM_018659.2	−1.7	−1.8	−2.0	−2.1	−1.6
MLKL	Mixed lineage kinase domain-like	NM_152649.1	−1.7	−1.6	−1.8	−2.0	−1.6
CTHRC1	Collagen triple helix repeat containing 1	NM_138455.2	−1.7	−1.8	−1.8	−2.0	−1.6
C6orf173	Chromosome 6 ORF 173	NM_001012507.1	−1.7	−1.6	−2.1	−1.8	−1.8
MGC40489	Hypothetical protein	XR_016048.1	−1.7	−1.8	−1.7	−2.0	−1.7
KDELR3	KDEL endoplasmic reticulum protein retention receptor 3, TV1	NM_006855.2	−1.7	−1.6	−1.8	−1.8	−2.0
TNFSF4	Tumour necrosis factor (ligand) superfamily, member 4	NM_003326.2	−1.7	−1.7	−1.7	−2.1	−1.9
AURKA	Aurora kinase A, TV5	NM_198436.1	−1.7	−1.7	−2.1	−1.9	−1.9
SMS	Spermine synthase	NM_004595.2	−1.7	−2.0	−1.8	−2.0	−1.7
RND3	Rho family GTPase 3	NM_005168.3	−1.7	−1.6	−2.0	−1.9	−1.7
CLDN5	Claudin 5 (transmembrane protein deleted in velocardiofacial syndrome)	NM_003277.2	−1.7	−1.4	−1.8	−2.1	−1.9
EDN1	Endothelin 1	NM_001955.2	−1.7	−1.7	−2.0	−1.7	−1.7
PVRL3	Poliovirus receptor-related 3	NM_015480.1	−1.7	−1.6	−2.0	−2.1	−1.8
LOX	Lysyl oxidase	NM_002317.3	−1.7	−1.9	−1.9	−2.0	−1.6
ICMT	Isoprenylcysteine carboxyl methyltransferase	NM_012405.3	−1.7	−1.6	−2.0	−1.8	−1.7
PRDX3	Peroxiredoxin 3, nuclear gene encoding mitochondrial protein, TV1	NM_006793.2	−1.7	−1.9	−1.8	−2.1	−1.6

Table 2. (Continued).

Gene symbol	Gene name	Accession number	X-bow	Disc	H	L	Y
TUBB6	Tubulin, β6 class V	NM_032525.1	−1.7	−2.2	−1.6	−1.8	−1.6
VAMP5	Vesicle-associated membrane protein 5 (myobrevin)	NM_006634.2	−1.7	−1.9	−1.9	−2.1	−1.6
MORF4L2	Mortality factor 4-like 2	NM_012286.1	−1.7	−1.8	−1.9	−2.2	−1.7
NOP56	NOP56 ribonucleoprotein homologue (yeast), TV1	NM_006392.2	−1.7	−1.8	−1.9	−2.1	−1.7
HNRPK	Heterogeneous nuclear ribonucleoprotein K, TV3	NM_031263.1	−1.7	−1.8	−1.8	−2.0	−1.9
RNF121	Ring finger protein 121, TV1	NM_018320.3	−1.7	−1.4	−2.0	−2.0	−1.8
KDELC2	KDEL (Lys-Asp-Glu-Leu) containing 2	NM_153705.4	−1.7	−1.7	−1.9	−2.2	−1.8
FJX1	Four jointed box 1 (*Drosophila*)	NM_014344.2	−1.7	−1.6	−2.0	−2.1	−1.9
DNMT1	DNA (cytosine-5-)-methyltransferase 1	NM_001379.1	−1.7	−1.4	−1.8	−2.0	−1.7
LOC729779	Misc_RNA (LOC729779)	XR_019592.2	−1.7	−2.0	−1.8	−1.6	−1.7
FABP5	Fatty acid binding protein 5 (psoriasis-associated)	NM_001444.1	−1.7	−1.6	−1.9	−2.0	−1.7
ZDHHC6	Zinc finger, DHHC-type containing 6	NM_022494.1	−1.7	−1.8	−1.9	−2.2	−1.7
IL1RL1	Interleukin 1 receptor-like 1 (IL1RL1), TV2	NM_003856.2	−1.7	−1.9	−1.8	−2.0	−1.7
EBNA1BP2	EBNA1 binding protein 2	NM_006824.1	−1.7	−1.8	−2.1	−2.1	−1.6
TFDP1	Transcription factor Dp-1	NM_007111.3	−1.7	−1.6	−1.8	−2.1	−1.7
PAICS	Phosphoribosylaminoimidazole succinocarboxamide synthetase, TV2	NM_006452.3	−1.7	−1.7	−2.0	−2.2	−1.6
CISD1	CDGSH iron sulfur domain 1	NM_018464.2	−1.7	−1.7	−2.2	−2.1	−1.7
LOC100129086	Similar to HIG1 domain family, member 1A	XM_001725669.1	−1.7	−2.1	−2.0	−2.1	−1.7
POLE4	Polymerase (DNA-directed), ε4, accessory subunit	NM_019896.2	−1.8	−1.8	−2.0	−2.0	−1.6
FER1L3	Fer-1-like 3, myoferlin (*Caenorhabditis elegans*), TV2	NM_133337.1	−1.8	−1.5	−1.9	−2.0	−1.9
PVRL3	Poliovirus receptor-related 3	NM_015480.1	−1.8	−1.9	−2.2	−2.2	−1.9
RANBP1	RAN binding protein 1	NM_002882.2	−1.8	−2.1	−2.2	−2.3	−1.8
RAB11A	RAB11A, member RAS oncogene family	NM_004663.3	−1.8	−1.5	−1.8	−2.0	−1.7
SLC38A1	Solute carrier family 38, member 1, TV1	NM_030674.3	−1.8	−1.7	−2.1	−2.0	−2.0
IL8	Interleukin 8	NM_000584.2	−1.8	−1.9	−2.1	−2.0	−1.7
LOC100132715	Misc_RNA	XR_039129.1	−1.8	−1.5	−1.9	−2.0	−1.6
LOC644330	Similar to tropomyosin 3 isoform 2	XR_017492.1	−1.8	−2.4	−2.0	−2.1	−1.7
ZNF185	Zinc finger protein 185 (LIM domain)	NM_007150.2	−1.8	−1.6	−1.9	−2.0	−1.7
COL13A1	Collagen, type XIII, α1, TV19	NM_080815.2	−1.8	−1.6	−2.1	−2.0	−1.8
PKD2	Polycystic kidney disease 2 (autosomal dominant)	NM_000297.2	−1.8	−1.6	−1.9	−2.0	−2.0
MAGED1	Melanoma antigen family D, 1, TV2	NM_006986.3	−1.8	−1.7	−1.9	−1.9	−2.3
POLE3	Polymerase (DNA directed), ε3 (p17 subunit)	NM_017443.3	−1.8	−1.6	−2.0	−2.1	−1.7
CORO1C	Coronin, actin binding protein, 1C, TV1	NM_014325.2	−1.8	−1.5	−1.8	−2.0	−1.8
LOC652481	Similar to mitochondrial import inner membrane translocase subunit Tim23	XM_941942.1	−1.8	−2.2	−1.9	−1.9	−1.7
SLFN11	Schlafen family member 11	NM_152270.2	−1.8	−1.4	−2.0	−1.9	−1.8
PRNP	Prion protein (PRNP), TV3	NM_001080121.1	−1.8	−1.7	−1.9	−2.0	−2.2
FRMD6	FERM domain containing 6	NM_152330.2	−1.8	−1.8	−2.1	−2.2	−1.9
PTS	6-pyruvoyltetrahydropterin synthase	NM_000317.1	−1.8	−1.8	−1.9	−2.0	−1.5
PECI	Enoyl-CoA δ isomerase 2 (ECI2), TV1	NM_006117.2	−1.8	−2.4	−2.2	−2.5	−1.9
MGAT2	Mannosyl-glycoprotein-acetylglucosaminyltransferase, TV2	NM_001015883.1	−1.8	−2.1	−1.6	−2.1	−1.6
ATP6V0E2	ATPase, H^+ transporting V0 subunit e2, TV1	NM_145230.2	−1.8	−1.5	−2.0	−1.9	−1.8
RPL6	Ribosomal protein L6, TV1	NM_001024662.1	−1.8	−2.0	−1.9	−2.2	−1.8
CGNL1	Cingulin-like 1	NM_032866.3	−1.8	−1.8	−2.2	−2.3	−2.0
LDHA	Lactate dehydrogenase A, TV2	NM_001135239.1	−1.8	−1.8	−2.0	−2.1	−1.9
PGK1	Phosphoglycerate kinase 1	NM_000291.2	−1.8	−1.9	−1.9	−2.2	−1.8
CCND3	Cyclin D3	NM_001760.2	−1.8	−1.6	−2.0	−2.0	−2.0
SFRS2	Serine/arginine-rich splicing factor 2	NM_003016.3	−1.8	−1.7	−2.3	−2.2	−1.9
F2RL1	Coagulation factor II (thrombin) receptor-like 1	NM_005242.3	−1.8	−1.8	−1.8	−2.2	−1.8
PLSCR4	Phospholipid scramblase 4	NM_020353.1	−1.8	−1.7	−1.8	−2.1	−1.6
KDELR3	KDEL endoplasmic reticulum protein retention receptor 3, TV2	NM_016657.1	−1.8	−2.0	−2.0	−2.2	−1.9

Table 2. (Continued).

Gene symbol	Gene name	Accession number	X-bow	Disc	H	L	Y
LOC653226	Similar to signal recognition particle 9 kDa protein (SRP9)	XM_927451.2	−1.8	−2.2	−1.8	−2.0	−1.5
LOC387882	Hypothetical protein	NM_207376.1	−1.8	−1.8	−2.1	−2.1	−1.7
PPM1F	Protein phosphatase, Mg^{2+}/Mn^{2+} dependent, 1F	NM_014634.2	−1.8	−1.4	−1.9	−2.1	−1.7
PRICKLE1	Prickle homologue 1 (*Drosophila*)	NM_153026.1	−1.8	−1.4	−2.0	−1.7	−1.8
TSPAN5	Tetraspanin 5	NM_005723.2	−1.8	−1.7	−2.0	−2.2	−1.6
PDCD6IP	Programmed cell death 6 interacting protein	NM_013374.3	−1.8	−1.7	−1.8	−2.2	−1.9
EFEMP1	EGF-containing fibulin-like extracellular matrix protein 1	NM_004105.3	−1.8	−3.0	−1.8	−2.2	−1.7
CDC20	Cell division cycle 20 homologue (*S. cerevisiae*)	NM_001255.2	−1.8	−1.9	−2.1	−1.8	−2.0
LOC642590	Misc_RNA	XR_037021.1	−1.8	−1.8	−1.8	−2.2	−1.7
PRKAG2	Protein kinase, AMP-activated, γ2 noncatalytic subunit, TVb	NM_024429.1	−1.9	−1.9	−2.0	−2.1	−2.0
MRPL39	Mitochondrial ribosomal protein L39, TV1	NM_017446.3	−1.9	−1.9	−1.9	−2.2	−1.7
TRAM2	Translocation associated membrane protein 2	NM_012288.3	−1.9	−1.5	−2.0	−2.1	−1.8
B4GALT5	UDP-Gal:βGlcNAc β 1,4- galactosyltransferase, polypeptide 5	NM_004776.2	−1.9	−1.8	−2.2	−2.4	−2.3
TUBA1A	Tubulin, α1a	NM_006009.2	−1.9	−2.0	−1.8	−2.3	−1.9
KPNA2	Karyopherin α2 (RAG cohort 1, importin α 1)	NM_002266.2	−1.9	−2.3	−2.0	−2.2	−1.9
FER1L3	Fer-1-like 3, myoferlin (*C. elegans*) (FER1L3), TV1	NM_013451.2	−1.9	−1.9	−1.8	−2.0	−2.0
NLGN1	Neuroligin 1	NM_014932.2	−1.9	−1.9	−2.3	−2.5	−2.0
ALDH3A2	Aldehyde dehydrogenase 3 family, member A2, TV2	NM_000382.2	−1.9	−1.9	−1.8	−2.1	−1.8
LOC732007	Similar to phosphoglycerate mutase 1	XR_015684.1	−1.9	−1.9	−1.8	−2.2	−2.0
C21orf63	Family with sequence similarity 176, member C	NM_058187.3	−1.9	−1.7	−2.2	−1.9	−1.7
MSRB3	Methionine sulfoxide reductase B3, TV1	NM_198080.2	−1.9	−2.1	−1.7	−2.0	−1.7
PLXNA2	Plexin A2	NM_025179.3	−1.9	−1.5	−2.1	−1.9	−1.9
UCHL3	Ubiquitin carboxyl-terminal esterase L3 (ubiquitin thiolesterase)	NM_006002.3	−1.9	−2.0	−2.3	−2.3	−2.0
MT1G	Metallothionein 1G	NM_005950.1	−1.9	−1.4	−2.0	−1.8	−1.8
NEXN	Nexilin (F actin binding protein), TV1	NM_144573.3	−1.9	−2.2	−2.1	−2.1	−1.9
CRIM1	Cysteine rich transmembrane BMP regulator 1 (chordin-like)	NM_016441.1	−1.9	−2.5	−2.0	−2.4	−1.9
LOC644774	Similar to phosphoglycerate kinase 1	XM_927868.1	−1.9	−2.3	−2.1	−2.4	−2.0
UBE2T	Ubiquitin-conjugating enzyme E2T (putative)	NM_014176.2	−1.9	−1.9	−2.0	−2.0	−1.8
LOC441019	Hypothetical LOC441019	XM_498969.2	−1.9	−1.5	−2.1	−2.1	−2.1
PGAM1	Phosphoglycerate mutase 1 (brain)	NM_002629.2	−1.9	−2.4	−1.8	−1.9	−1.6
LPHN2	Latrophilin 2	NM_012302.2	−1.9	−1.6	−2.1	−2.3	−1.9
EHD4	EH-domain containing 4	NM_139265.2	−1.9	−1.6	−1.9	−2.0	−1.7
MYOF	Myoferlin, TV1	NM_013451.3	−1.9	−1.8	−1.9	−2.2	−1.9
PTTG1	Pituitary tumour-transforming 1	NM_004219.2	−1.9	−2.2	−2.1	−2.1	−1.8
TUBA1C	Tubulin, α1c	NM_032704.2	−1.9	−2.0	−1.9	−2.2	−1.9
ANXA2	Annexin A2, TV2	NM_001002857.1	−1.9	−2.8	−2.2	−2.5	−1.8
FILIP1L	Filamin A interacting protein 1-like, TV3	NM_001042459.1	−1.9	−1.8	−2.1	−1.9	−2.0
TRIP6	Thyroid hormone receptor interactor 6	NM_003302.2	−1.9	−1.8	−2.1	−1.9	−1.9
GIMAP7	GTPase, IMAP family member 7	NM_153236.3	−1.9	−1.9	−2.1	−2.6	−2.0
PECI	Enoyl-CoA δ isomerase 2, TV1	NM_006117.2	−1.9	−1.9	−2.1	−2.1	−1.9
TMEM14A	Transmembrane protein 14A	NM_014051.3	−1.9	−2.1	−2.1	−2.3	−2.3
CALD1	Caldesmon 1 (CALD1), TV5	NM_033140.2	−2.0	−2.0	−2.3	−2.1	−2.0
LOC402221	Similar to actin α1 skeletal muscle protein	XM_938988.1	−2.0	−2.0	−1.8	−2.2	−2.2
CCND2	Cyclin D2	NM_001759.2	−2.0	−1.7	−1.9	−2.1	−2.1
PRNP	Prion protein (PRNP), TV2	NM_183079.2	−2.0	−2.0	−2.2	−2.2	−2.4
FRMD6	FERM domain containing 6, TV2	NM_152330.3	−2.0	−2.0	−2.0	−2.1	−1.9
EFHD2	EF-hand domain family, member D2	NM_024329.4	−2.0	−1.7	−2.2	−2.2	−2.0
AADACL1	Arylacetamide deacetylase-like 1	NM_020792.3	−2.0	−2.3	−2.2	−2.4	−2.2

Table 2. (Continued).

Gene symbol	Gene name	Accession number	X-bow	Disc	H	L	Y
TGM2	Transglutaminase 2, TV1	NM_004613.2	−2.0	−1.8	−2.3	−2.1	−1.9
CAV2	Caveolin 2 (CAV2), TV1	NM_001233.3	−2.0	−2.7	−2.3	−2.6	−2.0
NNMT	Nicotinamide *N*-methyltransferase	NM_006169.2	−2.0	−2.1	−2.2	−2.2	−2.0
UAP1	UDP-*N*-acteylglucosamine pyrophosphorylase 1	NM_003115.3	−2.0	−1.6	−2.2	−2.0	−1.9
TJP2	Tight junction protein 2 (zona occludens 2), TV2	NM_201629.1	−2.0	−1.8	−2.2	−2.0	−2.0
AURKA	Aurora kinase A, TV3	NM_198434.1	−2.0	−1.9	−2.2	−2.1	−2.1
CSTF3	Cleavage stimulation factor, 3′ pre-RNA, subunit 3, 77 kDa, TV2	NM_001033505.1	−2.0	−2.2	−2.1	−2.3	−1.9
PTPLA	Protein tyrosine phosphatase-like, member A	NM_014241.3	−2.0	−1.9	−2.1	−2.3	−2.0
CAV1	Caveolin 1, caveolae protein, 22 kDa	NM_001753.3	−2.0	−2.0	−2.3	−2.3	−1.9
EXT1	Exostosin 1	NM_000127.2	−2.0	−1.7	−2.0	−2.4	−2.2
CCNA2	Cyclin A2	NM_001237.2	−2.0	−1.9	−2.1	−1.9	−1.9
CD59	CD59 molecule, complement regulatory protein, TV2	NM_000611.4	−2.0	−1.5	−2.0	−2.1	−2.1
TUBB2C	Tubulin, β4B class IVb	NM_006088.5	−2.0	−1.9	−2.2	−2.4	−2.4
SFRS3	Splicing factor, arginine/serine-rich 3	NM_003017.3	−2.0	−2.0	−2.1	−2.2	−2.0
RAN	RAN, member RAS oncogene family	NM_006325.2	−2.0	−2.2	−2.3	−2.4	−2.0
ADAM9	ADAM metallopeptidase domain 9, TV1	NM_003816.2	−2.0	−2.8	−2.0	−2.3	−1.9
LRP8	Low density lipoprotein receptor-related protein 8, TV3	NM_017522.3	−2.0	−1.9	−2.2	−2.2	−2.2
MELK	Maternal embryonic leucine zipper kinase	NM_014791.2	−2.0	−2.0	−2.1	−2.3	−2.0
GALNT10	Polypeptide *N*-acetylgalactosaminyltransferase 10, TV2	NM_017540.3	−2.0	−1.9	−1.9	−2.0	−1.9
CBX6	Chromobox homologue 6	NM_014292.3	−2.0	−1.6	−2.3	−2.5	−2.0
CALM1	Calmodulin 1 (phosphorylase kinase, δ)	NM_006888.3	−2.0	−1.7	−2.3	−2.4	−2.1
PTTG1	Pituitary tumour-transforming 1	NM_004219.2	−2.1	−1.9	−2.1	−2.2	−1.8
IL8	Interleukin 8	NM_000584.2	−2.3	−2.9	−3.0	−3.2	−2.5
IL1RL1	Interleukin 1 receptor-like 1, TV2	NM_003856.2	−2.1	−2.0	−2.5	−2.5	−1.9
FZD4	Frizzled homologue 4 (*Drosophila*)	NM_012193.2	−2.1	−1.6	−2.0	−2.1	−2.1
GLCE	Glucuronic acid epimerase	NM_015554.1	−2.1	−2.0	−2.5	−2.7	−2.4
UBE2C	Ubiquitin-conjugating enzyme E2C, TV6	NM_181803.1	−2.1	−2.1	−2.0	−2.1	−1.9
FAM176A	Family with sequence similarity 176, member A, TV1	NM_001135032.1	−2.1	−2.1	−2.1	−2.2	−2.2
ICAM2	Intercellular adhesion molecule 2, TV1	NM_001099786.1	−2.1	−2.1	−2.4	−2.8	−2.1
TGM2	Transglutaminase 2, TV2	NM_198951.1	−2.1	−2.0	−2.5	−2.4	−2.0
EPHA2	EPH receptor A2	NM_004431.2	−2.1	−1.7	−2.0	−2.1	−2.0
FEN1	Flap structure-specific endonuclease 1	NM_004111.4	−2.1	−2.2	−2.6	−2.5	−2.2
ATP1B1	ATPase, Na^+/K^+ transporting, β1 polypeptide	NM_001677.3	−2.1	−2.0	−2.1	−2.6	−2.1
ODZ3	Odz, odd Oz/ten-m homologue 3 (*Drosophila*)	NM_001080477.1	−2.1	−1.9	−2.3	−2.5	−2.1
FILIP1L	Filamin A interacting protein 1-like, TV1	NM_182909.2	−2.1	−1.8	−2.1	−2.1	−1.9
NMT2	*N*-myristoyltransferase 2	NM_004808.1	−2.1	−2.1	−2.4	−2.5	−2.3
PHACTR2	Phosphatase and actin regulator 2, TV1	NM_001100164.1	−2.1	−1.9	−2.2	−2.5	−1.9
TUBA1B	Tubulin, α1b	NM_006082.2	−2.1	−1.9	−2.4	−2.1	−2.3
C20orf127	Chromosome 20 ORF 127	NM_080757.1	−2.1	−1.8	−2.7	−2.6	−2.0
NPFFR2	Neuropeptide FF receptor 2, TV1	NM_004885.1	−2.1	−2.1	−2.3	−2.2	−2.3
LIMA1	LIM domain and actin binding 1	NM_016357.3	−2.2	−2.1	−2.2	−2.2	−1.9
BASP1	Brain abundant, membrane attached signal protein 1	NM_006317.3	−2.2	−2.0	−2.4	−2.5	−2.2
TNFRSF12A	Tumour necrosis factor receptor superfamily, member 12A	NM_016639.1	−2.2	−1.9	−2.6	−2.2	−2.1
KRT7	Keratin 7	NM_005556.3	−2.2	−1.8	−2.2	−2.2	−2.0
NCAPG	Non-SMC condensin I complex, subunit G	NM_022346.3	−2.2	−2.1	−2.2	−2.3	−2.4
CCNA1	Cyclin A1	NM_003914.2	−2.2	−2.4	−2.4	−2.5	−2.5
DIO2	Deiodinase, iodothyronine, type II, TV3	NM_001007023.2	−2.2	−2.0	−2.1	−1.9	−2.2
DDAH1	Dimethylarginine dimethylaminohydrolase 1	NM_012137.2	−2.2	−2.1	−2.8	−2.6	−2.4
CAV1	Caveolin 1, caveolae protein, 22 kDa	NM_001753.3	−2.2	−2.4	−2.4	−2.7	−2.4
TYMS	Thymidylate synthetase	NM_001071.1	−2.2	−2.3	−2.4	−2.2	−2.0
GRB14	Growth factor receptor-bound protein 14	NM_004490.2	−2.2	−2.1	−2.5	−2.4	−2.1
CAV2	Caveolin 2, TV1	NM_001233.3	−2.2	−2.5	−2.3	−2.6	−2.2

Table 2. (Continued).

Gene symbol	Gene name	Accession number	X-bow	Disc	H	L	Y
MGLL	Monoglyceride lipase (MGLL), TV1	NM_007283.5	−2.2	−1.8	−2.1	−2.2	−2.1
FILIP1L	Filamin A interacting protein 1-like, TV2	NM_014890.2	−2.2	−1.8	−2.6	−2.5	−2.1
CEP55	Centrosomal protein 55 kDa	NM_018131.3	−2.3	−2.2	−2.2	−2.4	−2.4
CALD1	Caldesmon 1, TV3	NM_033157.2	−2.3	−2.8	−2.5	−2.3	−1.9
UBE2C	Ubiquitin-conjugating enzyme E2C, TV3	NM_181800.1	−2.3	−2.4	−2.4	−2.7	−2.2
MTE	Metallothionein E	NM_175621.2	−2.3	−2.0	−3.2	−2.4	−2.5
MCM4	Minichromosome maintenance complex component 4, TV1	NM_005914.2	−2.3	−2.2	−2.5	−2.6	−2.3
FABP4	Fatty acid binding protein 4, adipocyte	NM_001442.1	−2.3	−2.1	−2.2	−2.3	−2.5
PLOD2	Procollagen-lysine, 2-oxoglutarate 5-dioxygenase 2, TV2	NM_000935.2	−2.3	−2.2	−2.6	−2.8	−2.5
TXNRD2	Thioredoxin reductase 2, nuclear gene encoding mitochondrial protein	NM_006440.3	−2.4	−2.2	−2.9	−2.8	−2.4
LDLR	Low-density lipoprotein receptor (familial hypercholesterolaemia)	NM_000527.2	−2.4	−2.2	−2.7	−2.6	−2.5
GIMAP4	GTPase, IMAP family member 4	NM_018326.2	−2.5	−2.2	−2.6	−2.9	−2.8
PRC1	Protein regulator of cytokinesis 1, TV2	NM_199413.1	−2.5	−2.1	−2.2	−2.3	−2.2
MGLL	Monoglyceride lipase, TV1	NM_007283.5	−2.5	−2.8	−2.8	−2.8	−2.4
FKSG30	Actin-like protein	NM_001017421.1	−2.5	−2.4	−2.3	−2.6	−2.2
ALDH1A3	Aldehyde dehydrogenase 1 family, member A3	NM_000693.2	−2.5	−2.6	−2.6	−2.9	−2.6
CYR61	Cysteine-rich, angiogenic inducer, 61	NM_001554.3	−2.5	−2.1	−2.5	−2.3	−2.7
MAD2L1	MAD2 mitotic arrest deficient-like 1 (yeast)	NM_002358.2	−2.5	−2.7	−2.7	−2.6	−2.6
CCL15	Chemokine (C-C motif) ligand 15, TV1	NM_032964.2	−2.5	−2.2	−2.5	−2.3	−2.3
S1PR3	sSphingosine-1-phosphate receptor 3	NM_005226.2	−2.5	−2.0	−2.5	−2.4	−2.5
C6orf105	Chromosome 6 ORF 105	NM_032744.1	−2.5	−3.1	−2.7	−2.9	−2.6
TACSTD2	Tumour-associated calcium signal transducer 2	NM_002353.1	−2.6	−2.2	−2.6	−3.1	−2.7
MT1E	Metallothionein 1E	NM_175617.3	−2.7	−2.2	−3.1	−2.7	−2.2
PLOD2	Procollagen-lysine, 2-oxoglutarate 5-dioxygenase 2, TV1	NM_182943.2	−2.7	−3.1	−2.9	−3.4	−2.7
STC2	Stanniocalcin 2	NM_003714.2	−2.7	−2.2	−3.3	−3.0	−2.9
SDPR	Serum deprivation response (phosphatidylserine binding protein)	NM_004657.4	−2.8	−3.1	−3.2	−3.7	−3.0
PLOD2	Procollagen-lysine, 2-oxoglutarate 5-dioxygenase 2, TV2	NM_000935.2	−2.8	−2.4	−2.9	−3.0	−2.9
LOC399942	Similar to tubulin α-2 chain (α-tubulin 2), TV5	XM_934471.1	−3.0	−3.3	−2.9	−3.0	−2.8
CXCL1	Chemokine (C-X-C motif) ligand 1	NM_001511.1	−3.1	−3.0	−3.3	−3.2	−2.9
UHRF1	Ubiquitin-like with PHD and ring finger domains 1, TV1	NM_001048201.1	−3.2	−2.7	−3.4	−3.1	−3.5
PTGER4	Prostaglandin E receptor 4 (subtype EP4)	NM_000958.2	−3.3	−2.5	−3.4	−3.9	−3.4
MGC87042	Similar to six transmembrane epithelial antigen of prostate	XM_001128032.1	−3.4	−2.9	−3.7	−3.8	−3.4
TOP2A	Topoisomerase (DNA) II α 170 kDa	NM_001067.2	−3.5	−3.3	−3.4	−3.5	−3.4
LOC399959	Mir-100-let-7a-2 cluster host gene (nonprotein coding)	NR_024430.1	−3.6	−3.0	−4.2	−4.0	−3.9
STEAP1	Six transmembrane epithelial antigen of the prostate 1	NM_012449.2	−3.6	−3.5	−3.6	−4.0	−3.7
BMP4	Bone morphogenetic protein 4, TV3	NM_130851.1	−3.6	−2.8	−4.3	−3.8	−3.8
LOC158376	Hypothetical protein	XM_001129749.1	−3.9	−3.3	−3.1	−3.6	−3.6
DKK1	Dickkopf 1 homologue (*Xenopus laevis*)	NM_012242.2	−5.2	−4.0	−6.2	−6.0	−5.5
RGS4	Regulator of G-protein signalling 4	NM_005613.3	−7.6	−6.5	−9.9	−10.2	−9.0

Table 3. Fold changes in mRNA expression levels of genes involved in cell cycle progression.

Gene	X-bow	Disc	H	L	Y
H1F0	1.6	1.4	1.5	1.5	1.8
TUBB6	−1.3	−1.4	−1.4	−1.6	−1.4
CCT2	−1.4	−1.3	−1.5	−1.6	−1.4
TUBA1C	−1.4	−1.3	−1.7	−1.5	−1.5
DYNLL1	−1.4	−1.4	−1.6	−1.7	−1.3
H3F3B	−1.4	−1.4	−1.8	−1.7	−1.5
TUBA1A	−1.5	−1.4	−1.6	−1.6	−1.7
RBX1	−1.5	−1.4	−1.5	−1.8	−1.5
PCNA	−1.5	−1.6	−1.8	−1.8	−1.5
TCP1	−1.5	−2.1	−1.4	−1.8	−1.4
CCT6A	−1.5	−2.1	−1.5	−1.9	−1.4
BUB3	−1.5	−1.4	−1.5	−1.5	−1.4
CSE1L	−1.5	−1.2	−1.5	−1.7	−1.4
TUBB2A	−1.5	−1.5	−1.7	−1.5	−1.6
CDK6	−1.6	−1.3	−1.5	−1.5	−1.6
PPP2CA	−1.6	−1.6	−1.8	−1.9	−1.7
CKS1B	−1.6	−1.6	−1.7	−1.8	−1.6
AURKA	−1.7	−1.7	−2.1	−1.9	−1.9
TFDP1	−1.7	−1.6	−1.7	−1.9	−1.7
CCND2	−1.7	−1.7	−2.0	−2.2	−2.0
CCND3	−1.8	−1.6	−2.0	−2.0	−2.0
CDC20	−1.8	−1.9	−2.1	−1.8	−2.0
CCNB2	−1.9	−1.8	−1.8	−1.7	−1.9
PTTG1	−1.9	−2.2	−2.1	−2.1	−1.8
CCNA2	−2.0	−1.9	−2.1	−1.9	−1.9
RAN	−2.0	−2.2	−2.3	−2.4	−2.0
TUBA1B	−2.1	−1.9	−2.4	−2.1	−2.3
NCAPG	−2.2	−2.1	−2.2	−2.3	−2.4
CCNA1	−2.2	−2.4	−2.4	−2.5	−2.5
MAD2L1	−2.5	−2.7	−2.7	−2.6	−2.6
TOP2A	−3.5	−3.3	−3.4	−3.5	−3.4

Table 4. Fold changes in mRNA expression levels of genes involved in cytoskeletal dynamics and cell adhesion.

Gene	X-bow	Disc	H	L	Y
SYNM	2.4	2.1	2.0	2.2	2.4
MMP10	2.0	2.0	1.6	1.4	1.7
MMP1	1.7	1.9	1.3	1.4	1.3
ITGB4	1.7	1.8	1.7	1.7	1.6
JUN	1.6	1.5	1.4	1.4	1.5
RPS6KA5	1.6	1.4	1.5	1.4	1.8
AXIN2	1.5	1.5	1.4	1.4	1.5
MYLK	1.5	1.3	1.5	1.3	1.4
CSNK2A2	1.5	1.5	1.3	1.2	1.4
TUBB6	−1.3	−1.4	−1.4	−1.6	−1.4
CD44	−1.4	−1.6	−1.3	−1.7	−1.4
TUBA1C	−1.4	−1.3	−1.7	−1.5	−1.5
FLOT2	−1.4	−1.3	−1.6	−1.7	−1.5
MYL9	−1.4	−1.7	−1.5	−1.6	−1.3
TUBA1A	−1.5	−1.4	−1.6	−1.6	−1.7
EIF4G2	−1.5	−2.2	−1.5	−2.0	−1.5
SHC1	−1.5	−1.4	−1.1	−1.3	−1.4
ROCK2	−1.5	−1.2	−1.4	−1.6	−1.5
VCL	−1.5	−1.6	−1.4	−1.7	−1.6
ZYX	−1.5	−1.4	−2.0	−1.7	−1.7
TUBB2A	−1.5	−1.5	−1.7	−1.5	−1.6
ACTN4	−1.6	−1.3	−1.8	−1.7	−1.6
CAV2	−1.6	−1.5	−1.8	−1.8	−1.7
NES	−1.7	−1.5	−1.7	−1.8	−1.5
ACTR2	−1.7	−1.5	−1.6	−1.8	−1.5
GNG12	−1.7	−2.5	−1.6	−2.1	−1.6
TUBB6	−1.7	−2.2	−1.6	−1.8	−1.6
TUBG1	−1.7	−1.4	−1.6	−1.9	−1.6
IL8	−1.8	−1.9	−2.1	−2.0	−1.7
TUBA1A	−1.9	−2.0	−1.8	−2.3	−1.9
TJP2	−2.0	−1.7	−1.6	−1.7	−1.7
TUBA1B	−2.1	−1.9	−2.4	−2.1	−2.3
CAV1	−2.2	−2.4	−2.4	−2.7	−2.4
CXCL1	−3.1	−3.0	−3.3	−3.2	−2.9

Upon demonstrating the reproducibility and applicability of micropatterns to control cellular morphology, we utilized microarray technology to analyze how morphological restriction and unique cellular morphologies affect the HCAEC transcriptome. Our data indicate that morphological restriction (i.e. ability of the cell to spread) is a major regulator of endothelial gene expression patterns, as demonstrated by large-scale changes in gene expression after morphological restriction of HCAECs. Our data indicate that morphological restriction via micropattern adherence greatly increases the incidence of nuclear deformation in HCAECs. Given that large-scale cell shape changes results in a drastic condensation of chromatin as a result of lateral compressive force-induced nuclear orientation shifts and deformation [25], it is possible that restricting cell spreading affects the dynamic genome architecture in the nuclear space, thus regulating gene expression by modulating the geometric constraints that regulate dynamic chromatin positioning. We suspect that shape-induced gene expression changes are more complex than simply a consequence of nuclear deformation given that the transcriptome between each of the micropatterned shapes was remarkably similar, whereas the level of nuclear deformation varied drastically between the individual micropatterns. Indeed, although distinct cell shapes and cytoskeletal patterning have been reported to regulate mesenchymal progenitor lineage determination and endothelial cell chromatin condensation [14,25], we were very surprised to discover that shape induced gene expression patterns were remarkably constant across all altered cellular morphologies tested relative to each other. Moreover, considering a recent study suggesting that cell geometry does not regulate the adipogenic differentiation of mesenchymal stem cells [15], further follow-up studies are needed to determine how cellular geometry affects the phenotype of different cell types. Our data do not necessarily

Table 5. Fold changes in mRNA expression levels of genes involved in glycolysis and gluconeogenesis.

Gene	X-bow	Disc	H	L	Y
ENO1	−1.4	−1.2	−1.6	−1.5	−1.4
MDH1	−1.5	−1.5	−1.6	−1.8	−1.4
PGK1	−1.5	−1.5	−1.6	−1.9	−1.9
PGAM1	−1.6	−1.7	−1.6	−1.8	−1.5
TPI1	−1.6	−1.7	−1.5	−1.7	−1.5
LDHA	−1.6	−1.6	−1.9	−2.0	−1.8
PGAM4	−1.7	−1.8	−1.6	−1.9	−1.7

Table 6. Fold changes in mRNA expression levels of genes involved in TGFβ signalling.

Gene	X-bow	Disc	H	L	Y
HEY1	3.1	2.7	2.7	2.7	3.1
SMAD7	2.6	2.4	2.5	2.7	2.6
GDF15	2.1	2.2	2.0	1.9	2.1
BMP2	2.1	2.0	1.9	1.7	2.0
SMAD6	1.9	2.0	1.8	1.8	2.0
BMPR2	1.6	1.6	1.4	1.4	1.6
GADD45B	1.4	1.4	1.2	1.4	1.7
FKBP1A	−1.4	−1.6	−1.4	−1.8	−1.3
TGFB2	−1.5	−1.5	−1.4	−1.5	−1.5
SHC1	−1.5	−1.4	−1.1	−1.3	−1.4
SNAI2	−1.7	−1.6	−1.7	−1.8	−1.7
TGFBR2	−1.5	−1.4	−1.6	−1.9	−1.6
EDN1	−1.7	−1.7	−2.0	−1.7	−1.7
BMP4	−1.7	−1.7	−1.6	−1.5	−1.8
CAV1	−2.0	−2.0	−2.3	−2.3	−1.9

Table 7. Fold changes in mRNA expression levels of genes involved in Wnt signalling.

Gene	X-bow	Disc	H	L	Y
TCF4	1.7	1.8	1.5	1.6	1.7
RUVBL2	−1.4	−1.4	−1.6	−1.6	−1.2
SNAI2	−1.7	−1.6	−1.7	−1.8	−1.7
FZD4	−2.1	−1.6	−2.0	−2.1	−2.1
DKK1	−5.2	−4.0	−6.2	−6.0	−5.5

contradict the report of shape-induced differentiation in mesenchymal progenitor cells [14] but, instead, suggest that there are varying levels of responsiveness to morphology driven cellular outputs between different cell types (mesenchymal progenitor versus coronary artery endothelial cells). Cummulatively, our data suggest that the ability of HCAECs to spread (but not necessarily their particular morphology) dictates their genomics patterns. These data build on and corroborate the findings reported in earlier work indicating that endothelial spreading regulates cell fate decisions between proliferation and death [8,11].

Bioinformatics analysis of the microarray data revealed that the largest functional groupings of genes whose expression was altered upon morphological restriction were those involved in cell cycle regulation (30 genes) and cytoskeletal dynamics/cell adhesion (34 genes). Within the identified cell cycle regulators, a number of genes were strongly involved in spindle assembly, cell cycle phase transition, nucleocytoplasmic transport of cyclins and cyclin-dependent kinases, and chromosome condensation. With the exception of one gene (*H1F0*, which encodes for a histone protein), the expression the identified cell cycle-related genes was down-regulated, including the major cell cycle promoters *CDK6*, *CCNA1*, *CCNB2*, *CCND2* and *CCND3*. Considering the previously proposed impact of cell shape on chromosome condensation, we were intrigued at the down-regulation of genes involved in DNA accessibility, including condensin (*NCAPG*), topoisomerase II α (*TOP2A*), histone H3 (*H3F3B*) and histone H1 (*H1F0*). These particular changes could have a role in modulating global gene expression, lineage specification and the cellular physiology of endothelial cells and their progenitors. In mesenchymal progenitor cells, it has been reported that shape-induced contraction enhances c-Jun N-terminal kinase and extracellular-related kinase 1/2 activity in conjunction with wingless-type signalling [14]. Pathway analysis of the microarray data from the shape confirmed that HCAECs revealed shape-induced alterations in the expression of genes involved in Wnt signalling (up-regulation of *TCF4* and down-regulation of *RUVBL2*, *SNAI2*, *FZD4* and *DKK1*) and an up-regulation in *JUN* expression, indicating that similar changes in these signalling pathways likely occur when the endothelial cell morphology is altered. Additionally, the expression of several genes encoding members of the TGFβ signalling cascades was altered upon changes in HCAEC shape, including the ligands *BMP2*, *BMP4* and *TGFB2*, the type II receptor *BMPR2*, and the signalling effectors *SMAD6* and *SMAD7*. Given that aberrant TGFβ signalling is critically implicated in the progression of coronary artery disease and arteriosclerosis [31], it is possible that endothelial cell shape changes could initiate and/or exacerbate disease progression via alterations in the expression of key genes involved in these processes.

Materials and methods

Cell culture and treatments

Primary cultures of human coronary artery endothelial cells (HCAECs; < 5 passages; #PCS-100-020; ATCC, Manassas, VA, USA) were cultured in vascular cell basal media

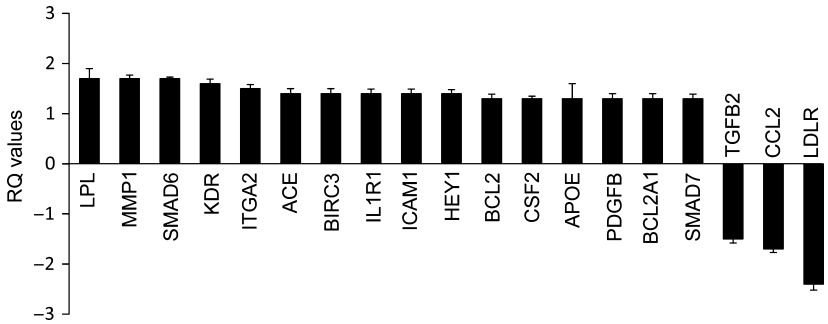

Fig. 6. Quantitative PCR confirmation of microarray data. Confirmatory quantitative PCR was performed on 19 genes whose expression was shown to be altered in the microarray data. Relative quantification (RQ) values are shown for each gene expression change. cDNA was obtained from normal and crossbow shape cells grown under standard culture conditions.

(#PCS-100-030; ATCC) supplemented with 0.2% bovine brain extract, 5 ng·mL^{-1} human epidermal growth factor, 10 mM L-glutamine, 0.75 units·mL^{-1} heparin sulfate, 1 μg·mL^{-1} hydrocortisone, 50 μg·mL^{-1} ascorbic acid, 2% fetal bovine serum and pen/strep. For serum starvation experiments, HCAECs were cultured in vascular cell basal media (#PCS-100-030; ATCC) supplemented with 10 mM L-glutamine, 0.75 units·mL^{-1} heparin sulfate, 1 μg·mL^{-1} hydrocortisone, 50 μg·mL^{-1} ascorbic acid and pen/strep for 48 h before RNA collection. For cell shape patterning, collagen I-coated coverslips and 96-well plates with micropatterns surrounded by non-adhesive surfaces (Cytoo Inc., Grenoble, France) were seeded with ~ 5000 or 50 000 HCAECs per well and coverslip, respectively, in accordance with the manufacturer's instructions. For the control, cells were seeded at low density approximately equal to that seen in the micropatterned conditions (to minimize cell-to-cell contacts) on collagen I-coated coverslips and 96-well plates. For all experiments, disc, crossbow, H, Y, and L adhesive micropatterns (1600 μm^2) plus controls were contained on the same chip or plate to reduce experimental variability.

Immunofluorescence

Micropatterned coverslips (Cytoo Inc.) were fixed in fresh 4% paraformaldehyde, blocked in 5% BSA plus 0.5% Tween-20, and incubated with 1 : 200 phospho-FAK (#3283; Cell Signaling, Danvers, MA, USA) antibody, 1 : 350 rhodamine-conjugated phalloidin (Cytoskeleton Inc., Denver, CO, USA) and 1 : 1000 DAPI. Anti-phospho-FAK was labelled with a FITC-conjugated secondary antibody and immunofluorescent images were captured in 0.1-μm Z-stacks using a C2SI scanning laser confocal microscope (Nikon, Tokyo, Japan). Images were equivalently processed in NIKON ELEMENTS 3.2, surface rendering images were obtained using IMARIS, version 6.0 (Bitplane AG, Zurich, Switzerland) and three-dimensional deconvolution was performed using Autoquant X3 (Media Cybernetics, Inc., Bethesda, MD, USA).

Quantification of actin fibre length

For each analysis, 11–14 images of each shape from the actin immunofluorescent images were utilized. Images were initially preprocessed by implementing contrast-limited adaptive histogram equalization, which enhances the contrast of the image in small regions rather than as a whole [32] (Fig. 2B). Images are rotated to have consistent orientation of the micropattern for all analyses. For automatic detection of actin fibres, we utilized the FIBERSCORE algorithm reported by Lichtenstein *et al.* [29], which bases the segmentation of fibres on the probability that a pixel neighbourhood belongs to a fibre. The output of the FIBERSCORE algorithm comprises a correlation image (Fig. 2C), which indicates pixels with higher probability of belonging to a fibre, and an orientation image (Fig. 2D), which indicates the orientation of the fibre at each pixel location. To remove fibres from the resulting FIBERSCORE output that are less correlated than other image regions, we performed a two-step post processing method: (a) remove pixels with correlation values below a predetermined threshold (Fig. 2E) and (b) skeletonize the fibre structures with combinations of the basic morphological operations erosion and opening [32] (Fig. 2F). The skeletonization process removes repetitive information within each detected fibre. Individual and median fibre lengths were obtained by measuring the processed fibre length in the skeletonized images.

Quantification of actin fibre orientation

For analysis of actin fibre orientation, each image was divided into nine separate tiles in the form of a 3 × 3 grid, thus providing information on where in the cell certain distributions of angles occur. Tiling allows for the option of local subcellular measurements of actin orientation, at the same time as gathering all information in the tiles provides a measure of the entire cell. For quantitative analysis of the 3 × 3 tiling, we implemented the two-sample KS test [30] to compare cell images within a single shape in terms of overall fibre orientation distributions. We used the KS test in two different methods to calculate the amount of difference between the distributions of fibre angles. In the first method, we compared the entire individual image to the cumulative tiling, providing a measure of the overall global difference in fibre distributions. The second method compared an individual image with the cumulative shape image on a tile-by-tile basis, providing a local measure of the

difference between individual cell distributions and the cumulative distributions. This tile-by-tile comparison is used to pinpoint similar regions between cell shapes that can be result in less uniqueness in global shape comparisons. Both methods count the number of null hypothesis rejections (at a significance level of 0.05) and normalize according to the number of KS tests.

Gene expression analysis

For each shape tested, as well as the nonrestricted controls, ~ 5000 HCAECs were grown in each well of a 96-well micropatterned plate. This was replicated in 16 independent wells per shape to minimize experimental error. Total RNA for each shape was isolated using the Purelink RNA Micro kit (Invitrogen, Grand Island, NY, USA) after 24 h of the cells adhering to the substrate. The isolated RNA from the replicates (5000 cells per shape multiplied by 16 independent replicates) were pooled, amplified and biotin-labelled using an Illumina TotalPrep RNA Amplification Kit (Illumina, San Diego, CA, USA). Some 750 ng of biotinylated aRNA was then briefly heat-denatured and loaded onto expression arrays to hybridize overnight. Following hybridization, arrays were labelled with Cy3-streptavidin and imaged using the Illumina ISCAN. Intensity values were transferred to GENESPRING GX software (Agilent Technologies Inc., Santa Clara, CA, USA) and data were filtered based on the quality of each call. Statistical relevance was determined using analysis of variance with a Benjamini Hochberg false discovery rate multiple testing correction ($P < 0.05$). Data were then limited by fold change analysis to statistically relevant data points demonstrating a two-fold or greater change in expression. Omics pathway analysis was performed with METACORE software (GeneGo, San Diego, CA, USA). Microarray data were publically deposited in Gene Expression Omnibus (standard growth conditions = accession number GSE43349; Serum starvation conditions = accession number GSE44168). For confirmation of microarray results, RNA from normal- and cross-bow-shaped cells was converted to cDNA using the Verso cDNA kit (Thermo-Scientific, Waltham, MA, USA) and quantitative PCR was performed using SYBR Green probes (Invitrogen) with an ABI7900HT real-time PCR instrument (Invitrogen).

Acknowledgements

Support for the present study was provided by a National Heart, Lung and Blood Institute grant HL098931 and internal support to B.A.B., a NASA EPSCoR award to New Mexico State University, and internal support from New Mexico State University to L.B.

References

1 Nieves BJ, D'Amore PA & Bryan BA (2009) The function of vascular endothelial growth factor. *BioFactors* **35**, 332–337.
2 Ingber DE (2008) Tensegrity and mechanotransduction. *J Bodyw Mov Ther* **12**, 198–200.
3 Ingber DE (2008) Tensegrity-based mechanosensing from macro to micro. *Prog Biophys Mol Biol* **97**, 163–179.
4 Klein-Nulend J, Bacabac RG, Veldhuijzen JP & Van Loon JJ (2003) Microgravity and bone cell mechanosensitivity. *Adv Space Res* **32**, 1551–1559.
5 Kher N & Marsh JD (2004) Pathobiology of atherosclerosis – a brief review. *Semin Thromb Hemost* **30**, 665–672.
6 Marshall KL & Lumpkin EA (2012) The molecular basis of mechanosensory transduction. *Adv Exp Med Biol* **739**, 142–155.
7 Sato M & Ohashi T (2005) Biorheological views of endothelial cell responses to mechanical stimuli. *Biorheology* **42**, 421–441.
8 Chen CS, Mrksich M, Huang S, Whitesides GM & Ingber DE (1997) Geometric control of cell life and death. *Science* **276**, 1425–1428.
9 Huang S, Chen CS & Ingber DE (1998) Control of cyclin D1, p27(Kip1), and cell cycle progression in human capillary endothelial cells by cell shape and cytoskeletal tension. *Mol Biol Cell* **9**, 3179–3193.
10 Huang S & Ingber DE (2000) Shape-dependent control of cell growth, differentiation, and apoptosis: switching between attractors in cell regulatory networks. *Exp Cell Res* **261**, 91–103.
11 Ingber DE, Prusty D, Sun Z, Betensky H & Wang N (1995) Cell shape, cytoskeletal mechanics, and cell cycle control in angiogenesis. *J Biomech* **28**, 1471–1484.
12 de Juan-Pardo EM, Hoang MB & Conboy IM (2006) Geometric control of myogenic cell fate. *Int J Nanomedicine* **1**, 203–212.
13 Lei Y, Zouani OF, Remy M, Ayela C & Durrieu MC (2012) Geometrical microfeature cues for directing tubulogenesis of endothelial cells. *PLoS ONE* **7**, e41163.
14 Kilian KA, Bugarija B, Lahn BT & Mrksich M (2010) Geometric cues for directing the differentiation of mesenchymal stem cells. *Proc Natl Acad Sci USA* **107**, 4872–4877.
15 Song W, Lu H, Kawazoe N & Chen G (2011) Adipogenic differentiation of individual mesenchymal stem cell on different geometric micropatterns. *Langmuir* **27**, 6155–6162.
16 Montalvo J, Spencer C, Hackathorn A, Masterjohn K, Perkins A, Doty C, Arumugam A, Ongusaha PP, Lakshmanaswamy R, Liao JK *et al.* (2013) ROCK1 & 2 perform overlapping and unique roles in angiogenesis

and angiosarcoma tumor progression. *Curr Mol Med* **13**, 205–219.

17 Sims JR, Karp S & Ingber DE (1992) Altering the cellular mechanical force balance results in integrated changes in cell, cytoskeletal and nuclear shape. *J Cell Sci* **103**, 1215–1222.

18 Jean RP, Gray DS, Spector AA & Chen CS (2004) Characterization of the nuclear deformation caused by changes in endothelial cell shape. *J Biomech Eng* **126**, 552–558.

19 Martins RP, Finan JD, Guilak F & Lee DA (2012) Mechanical regulation of nuclear structure and function. *Annu Rev Biomed Eng* **14**, 431–455.

20 Thomas CH, Collier JH, Sfeir CS & Healy KE (2002) Engineering gene expression and protein synthesis by modulation of nuclear shape. *Proc Natl Acad Sci USA* **99**, 1972–1977.

21 Lanctot C, Cheutin T, Cremer M, Cavalli G & Cremer T (2007) Dynamic genome architecture in the nuclear space: regulation of gene expression in three dimensions. *Nat Rev Genet* **8**, 104–115.

22 Misteli T (2007) Beyond the sequence: cellular organization of genome function. *Cell* **128**, 787–800.

23 Maniotis AJ, Chen CS & Ingber DE (1997) Demonstration of mechanical connections between integrins, cytoskeletal filaments, and nucleoplasm that stabilize nuclear structure. *Proc Natl Acad Sci USA* **94**, 849–854.

24 Le Beyec J, Xu R, Lee SY, Nelson CM, Rizki A, Alcaraz J & Bissell MJ (2007) Cell shape regulates global histone acetylation in human mammary epithelial cells. *Exp Cell Res* **313**, 3066–3075.

25 Versaevel M, Grevesse T & Gabriele S (2012) Spatial coordination between cell and nuclear shape within micropatterned endothelial cells. *Nat Commun* **3**, 671.

26 Gupta S, Marcel N, Sarin A & Shivashankar GV (2012) Role of actin dependent nuclear deformation in regulating early gene expression. *PLoS ONE* **7**, e53031.

27 Matonoha P & Zechmeister A (1978) Scanning electron microscopic observation of intimal surface of normal and atherosclerotic arteries. *Acta Morphol Acad Sci Hung* **26**, 173–184.

28 Levesque MJ, Liepsch D, Moravec S & Nerem RM (1986) Correlation of endothelial cell shape and wall shear stress in a stenosed dog aorta. *Arteriosclerosis* **6**, 220–229.

29 Lichtenstein N, Geiger B & Kam Z (2003) Quantitative analysis of cytoskeletal organization by digital fluorescent microscopy. *Cytometry A* **54**, 8–18.

30 Massey F (1957) The kolmogorov-smirnov test for goodness of fit. *J Am Stat Assoc* **46**, 68–78.

31 Toma I & McCaffrey TA (2012) Transforming growth factor-beta and atherosclerosis: interwoven atherogenic and atheroprotective aspects. *Cell Tissue Res* **347**, 155–175.

32 Woods RGR (2002) Digital Image Processing, Vol. **2**. Prentice Hall, Upper Saddle River, NJ.